



FACULTY  
OF SCIENCE

# X-Ray Tomography on Intestine Samples

Julia Katharina Rogalinski

---

Thesis submitted for the degree of Master of Science  
Project duration: 4 months (30 ECTS)  
Autumn semester 2022

Supervisor: Dr. Pablo Villanueva Perez  
Co-supervisor: Dr. Martin Bech

Department of Physics  
Division of Synchrotron Radiation Research  
Date of examination: 11th of January 2023



# Abstract

Enteric neuropathy describes a disease of the bowel caused by anomalies in the enteric nervous system. Patients suffering from this disease have symptoms including nausea, vomiting, diarrhea and pain. As enteric neuropathy is not well understood yet, its diagnosis is a non-trivial task.

Research on the enteric nervous system is needed in order to gain a better understanding of this disease, making a correct diagnosis and targeted treatment possible. Thus, this thesis presents the investigation of nervous cells in the bowel and different setups that can be used for this purpose. More specifically, this involves the recording of high-resolution 3D images, with the ultimate aim to segment the ganglia, that are made up of neurons, in the intestinal samples to determine their volumes and compare the ganglia volumes of samples from healthy with those of diseased patients. In order to do this, X-ray tomography based on absorption and phase contrast was performed.

This master thesis presents the comparison of two experimental setups, namely a lab based micro-CT in Lund, Sweden and the TOMCAT beamline at the Paul-Scherrer-Institut in Villigen, Switzerland, that were used to carry out these studies. It was concluded that the setups could not be compared in terms of contrast-to-noise ratio, as their determination was not successful. Regarding the resolution, it was found that the micro-CT setup is appropriate to perform overview scans of the sample, but its overall resolution is not high enough for the successful segmentation of the ganglia. In contrast, the TOMCAT setup delivered a resolution sufficient for the ganglia's segmentation. The visibility of the ganglia could be significantly improved by applying phase retrieval, using the *Paganin* algorithm, to the datasets before their reconstruction due to this procedure enhancing the contrast. A reconstruction of the TOMCAT data with a self-developed script was conducted and compared to the reconstruction that was done directly at the beamline. It was found that the self-developed reconstruction was successful overall, but not optimal when it came to applying the *Paganin* algorithm, leading to an ambiguous separation between tissue and background. Furthermore, the optimal  $\delta/\beta$  ratio for the phase retrieval reconstruction at the micro-CT setup was confirmed to be 217.6. After these preparations to find the optimal conditions for the segmentation of ganglia, the volumes of the ganglia, remaining biological tissue and background were determined to be  $0.011 \text{ mm}^3$ ,  $0.44 \text{ mm}^3$  and  $0.067 \text{ mm}^3$  in a  $0.5 \text{ mm}^3$  volume of one sample. The segmentation and subsequent determination of the volumes of further ganglia will pave the way for gaining a deeper knowledge of enteric neuropathy.

## Acknowledgements

First, I would like to express my appreciation to Pablo Villanueva Perez for the supervision of this thesis, for his support with all the questions I had and feedback throughout my complete writing process.

I am also grateful to my second supervisor Martin Bech, who gave me the possibility to collect the data for this thesis and always answered my questions.

I would also like to thank Zisheng Yao for taking time to help me whenever I had challenges with the analysis of my data.

Special thanks to my German office mates Robin Krüger and Till Dreier for introducing me to the lab setup in Lund, their patience in helping me with any problems I had to face, their emotional support and all the funny conversations we had.

I would like to acknowledge Bodil Ohlsson for her help and patience with explaining the medical background of this project to me.

I also want to thank the people from the Paul-Scherrer-Institut for helping with acquiring the synchrotron data. I had the pleasure of working with Niccolò Peruzzi and Sahel Ganji at the beamtime. Thanks for the good talks and insights in your tastes of music.

Lastly, I would like to extend my thanks to my friends, my Haralds fellows and family for always having an open ear for me.

# Contents

<b>Abstract</b>	<b>I</b>
<b>Acknowledgements</b>	<b>II</b>
<b>Contents</b>	<b>III</b>
<b>List of Figures</b>	<b>V</b>
<b>List of Tables</b>	<b>V</b>
<b>Acronyms</b>	<b>VI</b>
<b>1 Introduction</b>	<b>1</b>
<b>2 Theoretical Background</b>	<b>3</b>
2.1 X-Rays . . . . .	3
2.1.1 Interaction with Matter . . . . .	3
2.1.2 Contrast Mechanisms . . . . .	4
2.1.3 Resolution and Dose . . . . .	8
2.1.4 X-Ray Sources . . . . .	9
2.2 Tomography . . . . .	12
2.2.1 Fourier Slice Theorem . . . . .	13
2.2.2 Filtered Backprojection . . . . .	14
2.2.3 Corrections . . . . .	14
<b>3 Methods</b>	<b>15</b>
3.1 Sample . . . . .	15
3.2 Data Acquisition . . . . .	15
3.2.1 Micro-CT . . . . .	15
3.2.2 TOMCAT Beamline . . . . .	16
3.3 Data Analysis . . . . .	19
3.3.1 Phase Retrieval with TIE . . . . .	19
3.3.2 3D Image Reconstruction of Micro-CT Data . . . . .	20
3.3.3 3D Image Reconstruction of TOMCAT Data . . . . .	20
3.4 Image Segmentation . . . . .	21
<b>4 Results</b>	<b>23</b>
4.1 Image Reconstructions of Selected Slices . . . . .	23
4.2 Comparison of Setups . . . . .	26
4.3 Optimization of Phase Contrast for Micro-CT . . . . .	29
4.4 Segmentation of Ganglia . . . . .	31
<b>5 Discussion</b>	<b>33</b>
5.1 Comparison of Setups . . . . .	33
5.2 Comparison of Contrasts . . . . .	35
5.3 Evaluation of Self-Developed Reconstruction . . . . .	35
5.4 Optimization of Phase Contrast for Micro-CT . . . . .	36

5.5 Segmentation of Ganglia . . . . .	37
<b>6 Conclusion</b>	<b>38</b>
<b>7 Outlook</b>	<b>40</b>
<b>References</b>	<b>41</b>
<b>Appendix</b>	<b>44</b>

## List of Figures

1	Location of enteric nervous system. . . . .	1
2	Refractive-index decrement, absorption index and transmission . . . . .	4
3	Attenuation and phase shift . . . . .	5
4	Diffraction regimes . . . . .	7
5	Required and maximum tolerable dose . . . . .	8
6	Brightness . . . . .	10
7	Laboratory X-ray source . . . . .	10
8	Construction of a synchrotron . . . . .	12
9	Working principle of tomography . . . . .	12
10	Experimental setup of the micro-CT . . . . .	15
11	Experimental setup at TOMCAT . . . . .	17
12	Overview of sample . . . . .	23
13	Reconstructed images without phase retrieval . . . . .	24
14	Reconstructed mages with phase retrieval . . . . .	25
15	Segmented blood vessel . . . . .	26
16	3D blood vessel from direct TOMCAT reconstruction with $\delta/\beta = 217.6$ . . . . .	27
17	Ganglia within the images . . . . .	29
18	Reconstructed images of micro-CT setup with different $\delta/\beta$ ratios . . . . .	30
19	Segmentation of ganglia . . . . .	32
20	Discussion of CNR in case of absorption contrast . . . . .	34
21	Discussion of CNR in case of phase contrast . . . . .	44

## List of Tables

1	Parameters used at micro-CT . . . . .	16
2	Parameters used at TOMCAT . . . . .	18
3	Contrast-to-noise ratios without phase retrieval . . . . .	27
4	Contrast-to-noise ratios with phase retrieval . . . . .	28
5	SNR for different $\delta/\beta$ ratios . . . . .	31

## Acronyms

$\beta$  Absorption index. 3–5

$\delta$  Refractive-index decrement. 3–5, 7, 19

**BW** Bandwidth. 9

**CNR** Contrast-to-noise ratio. V, 2, 23, 26–28, 31, 33, 34, 36, 38, 44

**DOF** Depth of focus. 18

**ENS** Enteric nervous system. 1, 17, 33, 37–40

**FBP** Filtered backprojection. 14

**FoV** Field of view. 16, 18, 23

**FT** Fourier Transform. 13, 14, 19, 20

**FWHM** Full width at half maximum. 31

**IBS** Irritable bowel syndrome. 1

**ID** Insertion device. 11

**LINAC** Linear accelerator. 11, 12

**NA** Numerical aperture. 18

**PSI** Paul-Scherrer-Institut. 15

**RF** Radio frequency. 11

**ROI** Region of interest. 17, 21, 35, 40

**SD** Self-developed. 23–28, 33, 35, 36

**SLS** Swiss Light Source. 16, 38

**SNR** Signal-to-noise ratio. V, 8, 31, 37, 38

**TIE** Transport-of-intensity equation. 7, 19



# 1 Introduction

Gastrointestinal disorders are a common type of disease with a non-negligible impact on the life quality of those affected [1]. Several clinical pictures are summarized under the term "gastrointestinal disorders", which refers to dysfunctions of the gastrointestinal tract. Symptoms may include abdominal pain, nausea, vomiting and diarrhea, with body weight loss as a possible consequence. If no organic causes for the occurring symptoms are found by standard examination methods, the diagnosis of irritable bowel syndrome (IBS) is made. However, IBS might be a wrong diagnosis, as was shown by B. Ohlsson et al. [2] on a specific case, which deals with a patient who was diagnosed with IBS at first. Due to additional investigations of colon tissue of the patient, obtained by biopsy, a specific reason for the patient's symptoms was found: alterations within the enteric nervous system (ENS) were observed, leading to the diagnosis of enteric neuropathy.

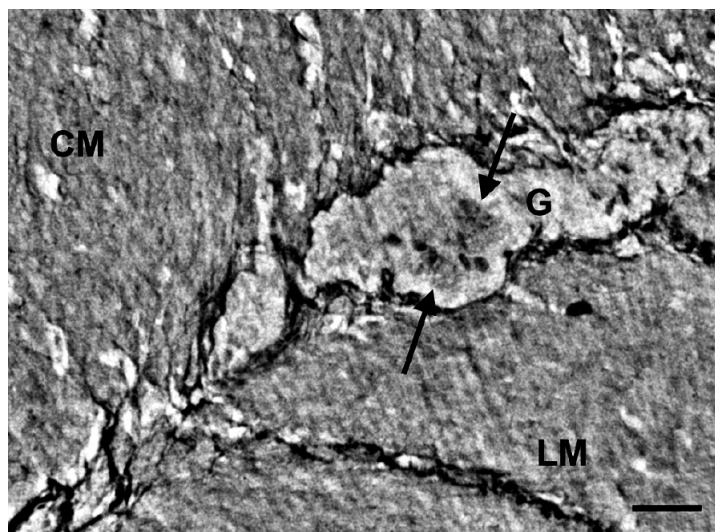


**Figure 1:** The location of the ENS between the circular (CM) and longitudinal (LM) muscle layer in the bowel. Part of the ENS consists of ganglia (G), which are made up of neurons (arrows). The size bar corresponds to 25  $\mu\text{m}$  [3].

A part of the ENS, i.e. a ganglion (G) which is made up of neurons (arrows), is located between a circular (CM) and longitudinal (LM) muscle layer within the bowel, as can be seen in Figure 1. The ENS controls the bowel's movement and disturbances in these movements due to alterations in the ENS can cause the symptoms described above [3]. As of now, it can be assumed that a large number of cases of enteric neuropathy is unknown. A better understanding of this disease and a correct diagnosis are important to provide treatment. In order to improve the understanding of this disease, morphological studies of the ENS of patients with and without its alterations are needed. More specifically, this involves the comparison of the volumes of the ganglia of the different patients.

So far, the standard procedure to examine the ENS is the combination of light microscopy with immunohistochemistry. The latter describes the process of visualizing certain parts of the sliced sample by using specific antibodies. More details on this procedure can be found in [4]. The problem with this method is that the ENS is possibly spread over several slices, motivating the need for 3D images. However, this is difficult to realize because the slices are likely to show artefacts due to imperfect slicing and the overall process is very time-consuming. An alternative approach is given by the use of X-ray tomography,

which has the advantage of directly delivering 3D images without the requirement of sectioning the sample. The obtained 3D images can subsequently be segmented to determine the volumes of the ganglia [2, 3].

In this master thesis, the whole chain of a tomographic experiment was performed: The data was acquired with tomographic setups (micro-CT and synchrotron), followed by the 3D reconstruction of the images using two contrast mechanisms: absorption and phase contrast. The former takes into account the attenuation of light, whereas the latter is caused by a shift in phase as light passes through the sample. The obtained images were segmented in order to study different parts of the sample in detail.

This master thesis presents 3D images of intestine samples with the overall aim of finding mandatory requirements to be able to visualize the ganglia. More specifically, this involves addressing the question if synchrotron radiation is needed to resolve the ganglia with a resolution high enough to perform segmentation on the images and for what purposes lab based X-ray sources can be used. Furthermore, the contrast-to-noise ratios (CNRs) delivered by the two different setups are compared and the question if phase contrast is needed for the ganglia's visualization is being dealt with. This is followed by discussing how the phase contrast can be optimized. Lastly, image segmentation was performed in order to determine the volumes of the ganglia in one sample.

It was found that synchrotron radiation is no requirement but advantageous in terms of lowering exposure time and hence radiation dose. However, what is needed is a setup that delivers a resolution in the range of  $4.875\ \mu\text{m}$ . The lab based X-ray source can be used to perform overview scans for the overall location of the ganglia within the sample, but its resolution is not high enough to perform a sufficient segmentation of the ganglia. The contrast-to-noise ratio (CNR) was significantly higher for the lab based X-ray source in case of absorption contrast images, but it was concluded that the determined CNRs are not reliable and should consequently not be used to compare the two setups (Section 5.1). The phase contrast was found to be necessary to improve the contrast between ganglia and surrounding tissue, making a segmentation less ambiguous (Section 5.2). In addition to the reconstruction of the data acquired by the synchrotron directly at the beamline, the acquired data was also reconstructed using a self-developed Python code. This self-developed approach was evaluated to be working overall, but delivering less optimal results than the direct reconstruction at the beamline when it came to separating the biological tissue from the background (Section 5.3). The phase contrast of the lab based X-ray source was optimized by changing the  $\delta/\beta$  ratio and the value of 217.6 was found to be best (Section 5.4). The volume of the ganglia was determined to be  $0.011\ \text{mm}^3$ , whereas the volumes of the remaining biological tissue and background were found to be  $0.44\ \text{mm}^3$  and  $0.067\ \text{mm}^3$ , respectively, and the impact of these results on medical research was discussed (Section 5.5).

## 2 Theoretical Background

### 2.1 X-Rays

X-rays can be used to obtain 3D images in a non-destructive way due to their energy, motivating the main reason for their application. As they have a higher penetration depth compared to photons with lower energies, it is possible to image the complete object of question. That means that there is no need to section the object and it can be investigated in a non-destructive way. Furthermore, their short wavelengths lead to higher spatial resolutions (i.e. resolutions in the order of their wavelength). Therefore, the needed high-resolution images can be obtained using X-ray imaging techniques [5, 6].

Imaging techniques map the interactions between light and matter. Thus, to understand their performance and limitations, these interactions should be understood first. In the following lines, X-ray interactions with matter are described.

#### 2.1.1 Interaction with Matter

The three interactions of X-rays with matter are elastic and inelastic scattering and absorption. Scattering takes place due to the fact that X-rays (and photons in general) couple to charges. As a consequence, their electric field interacts with electrons in matter. In the case of elastic scattering, no energy is transferred from the photon to the electron, meaning that the photon (as an electromagnetic wave) is scattered by the electron with the same wavelength as the incident one. For inelastic scattering this is not true anymore. Part of the photon's energy is transferred to the electron, hence accelerating it, with a lower energy (larger wavelength) of the scattered photon as a consequence. Furthermore, the incident and scattered wave have no phase relationship anymore, which is why this process can also be referred to as incoherent scattering [7, 8].

If a photon is absorbed by an atom, a core electron (photo electron) will be ejected and the photon will not transmit any further through the matter as a consequence. This leaves the atom in an unstable state, which is why the created hole is refilled by another electron from a shell further outside. The energy that is released in this process leads to either the emission of characteristic X-rays or an Auger electron [8].

Which interaction is dominant depends on what atoms the matter is made of and the photon's energy. In general, absorption is dominant for lower energies (up to approximately 10 keV for carbon), whereas inelastic scattering becomes dominant for higher energies [8].

Absorption and scattering both contribute to the so called refraction, which is a formalism describing the deflection of light from its original direction when it passes through different kinds of matter. That is because each medium has a specific refractive index  $n$  that is defined in Equation (1) [9].

$$n = n_R + in_I = 1 - \delta + i\beta \quad (1)$$

From this expression it can be seen that the real part  $n_R$  (imaginary part  $n_I$ ) is defined as  $1-\delta$  ( $\beta$ ). The parameter  $\delta$  is proportional to the electron density, describes the scattering properties of a specific material and is called refractive-index decrement, whereas  $\beta$  is the absorption index. Both, the contributions from  $\beta$  and  $\delta$  can be used to make contrast in imaging visible, as will be described in Section 2.1.2 [9, 10].

The refractive-index decrement and absorption index both depend on the photon energy

$E$ :  $\delta$  ( $\beta$ ) scales as  $E^{-2}$  ( $E^{-4}$ ). That means that  $\beta$  decreases much faster when increasing the energy compared to  $\delta$ . This can be seen for the example of  $C_{12}H_{53}O_{18}$  (biological sample) in Figure 2 [6].

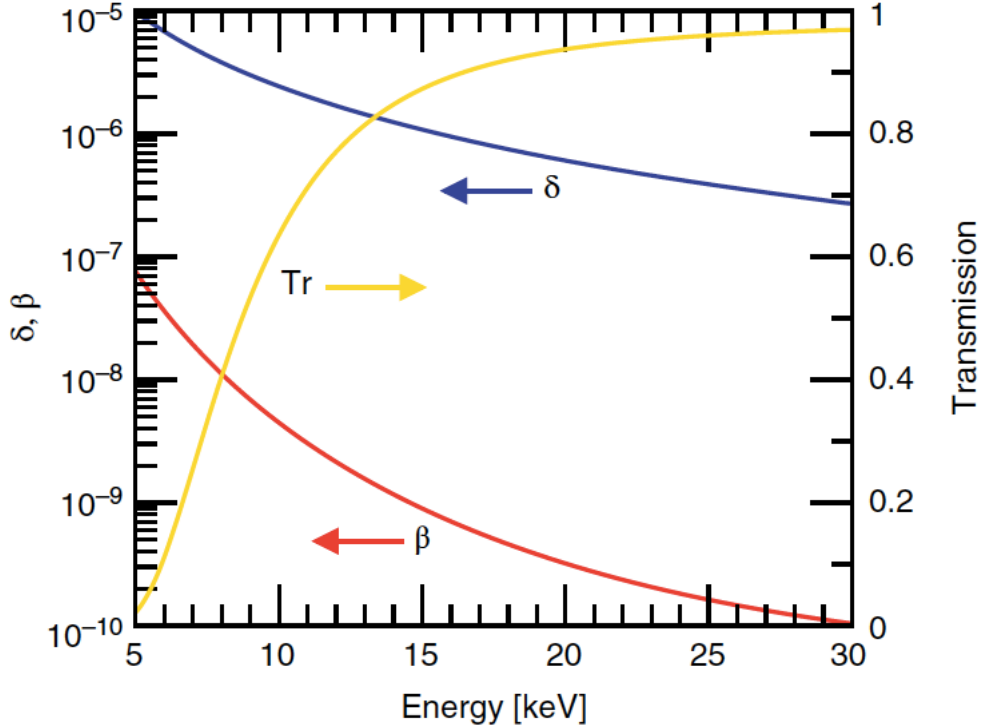


**Figure 2:** Values of refractive-index decrement  $\delta$ , absorption index  $\beta$  and transmission Tr for energies ranging from 5 to 30 keV for a 1 mm thick sample of flesh ( $C_{12}H_{53}O_{18}$ ) [6].

The blue (red) curve shows the decrease of  $\delta$  ( $\beta$ ) with increasing energies. It can be seen that the decrease of  $\beta$  is much steeper, making the contributions of  $\delta$  more dominant. At the same time the transmission (yellow) increases because of the decreasing absorption. That means that the deposited dose, which is defined as absorbed energy per mass, will decrease for higher energies, making radiation damage less probable, as will be discussed in Section 2.1.3 [6, 11].

### 2.1.2 Contrast Mechanisms

In order to make objects and their internal structures visible, a contrast mechanism is needed. Contrast enables mapping the interactions between X-rays and matter in order to image the physical world. Considering for example absorption contrast, one can detect the intensity of the attenuated beam after it passed through a sample. This attenuation is described by the Beer-Lambert law, as shown in Equation (2) [8].

$$I = I_0 \cdot \exp(-\mu z) \quad (2)$$

Here,  $I$ ,  $I_0$ ,  $\mu$  and  $z$  refer to the attenuated intensity, initial intensity, absorption coefficient and sample thickness, respectively. The absorption coefficient  $\mu$  is connected to the

absorption index  $\beta$  via Equation (3) with the wave vector  $k = 2\pi/\lambda$  [9].

$$\mu = 2\beta k = \frac{4\pi}{\lambda}\beta \quad (3)$$

The absorption of light, i.e. its attenuation while passing through a sample, becomes apparent in the amplitude of the lights' wave function. As light consists of electromagnetic waves, it can be described as propagating through matter as  $e^{inkz} = e^{-\beta kz} e^{i(1-\delta)kz}$  [10]. The first exponential term contains the absorption index and describes the attenuation of the wave's amplitude. This attenuation can be seen in Figure 3 as a wave passes through medium [9].

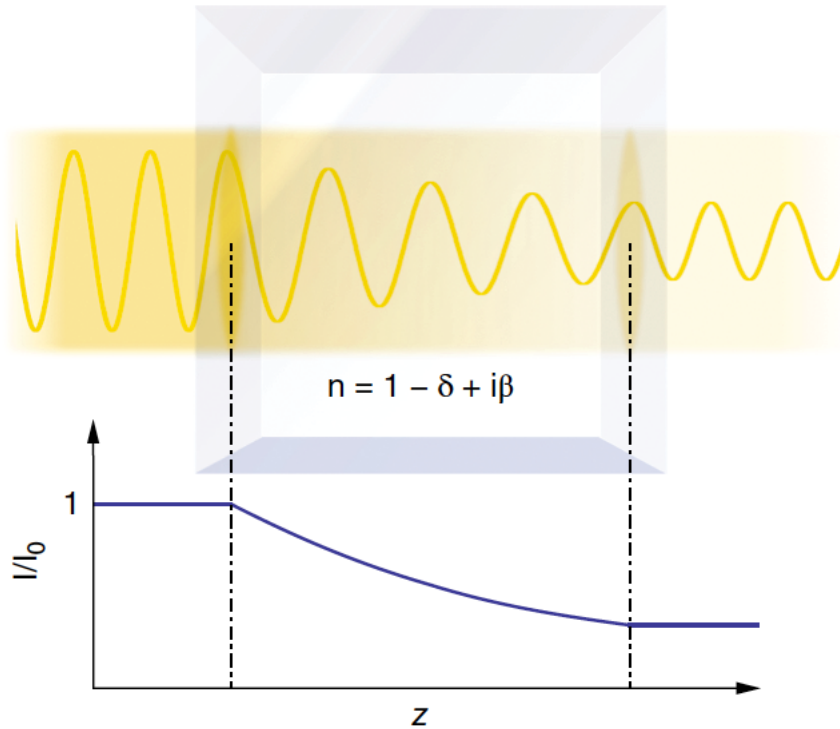


**Figure 3:** A wave passes through a medium of thickness  $z$ , leading to a decrease in its amplitude and intensity due to absorption and increase in wavelength due to phase shift in  $\delta$  [9].

What is detected in imaging experiments in the end is the intensity of the light, which is proportional to the wave's amplitude squared and the decrease in intensity due to absorption is shown in the graph on the bottom in Figure 3 [9].

The main problem with absorption contrast is that it is low for low  $Z$  materials or materials that have similar absorption properties, such as biological tissue. To overcome this problem, one can use lower photon energies because the absorption is dominant in that regime as was shown in Figure 2. However, as was discussed in Section 2.1.1, this will increase the radiation damage [6].

An alternative approach is to use phase contrast, which is a contrast mechanism based on  $\delta$ . When an electromagnetic wave passes through medium, a phase shift in  $\delta$  takes place. This phase shift is induced when a wave passes through different types of media because each medium has a different refractive index  $n$ . What happens in detail is that the phase velocity ( $v_p$  in Equation (4) [9]) of the wave in the medium increases, leading

to a larger wavelength as can be seen in Figure 3. The phase velocity is the velocity of the peaks and troughs of the individual wave, not to be confused with the group velocity  $v_g$ , which is the velocity of the overall wave (its envelope) [6, 9].

$$v_p = \frac{c}{n} \quad (4)$$

As  $n < 1$  for X-rays ( $n$  is energy dependent),  $v_p$  will be greater than the speed of light  $c$ , leading to a phase shift as described above [6]. This does not contradict special relativity, as  $v_g$  is still smaller than  $c$  [9].

In addition to this, the wave is deflected horizontally and/or vertically from its original path by an angle  $\alpha$ , which is connected to the phase  $\phi(x, y)$  as [5]:

$$\alpha_x = \frac{\lambda}{2\pi} \frac{\partial \phi(x, y)}{\partial x} \quad (5)$$

and

$$\alpha_y = \frac{\lambda}{2\pi} \frac{\partial \phi(x, y)}{\partial y}. \quad (6)$$

Behind the medium, the wave will interfere constructively or destructively with the reference wave, creating fringes due to the different phase velocities and deflection angles. Depending on the Fresnel number  $F_0$  (Equation (7) [6]) there will be more or less fringes present and it can be distinguished between different regimes. The regime in which the experiment takes place is determined by the sample-detector distance  $z$ , scattering object dimension  $a$  and wavelength  $\lambda$  [5, 6].

$$F_0 = \frac{a^2}{z\lambda} \quad (7)$$

The different regimes are illustrated in Figure 4. Whereas the left hand side shows the information obtained by the attenuation of the light, the right hand side shows that the shapes of the sample's features are lost and the information of the original image has to be recovered by using phase retrieval, as will be discussed in Section 3.3.1.

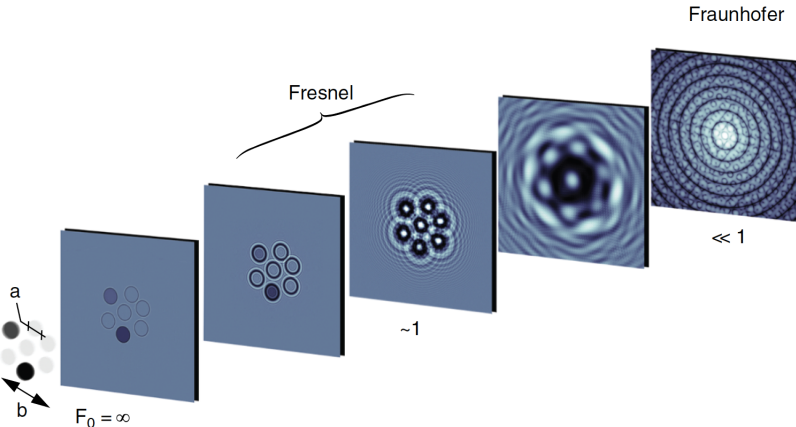


**Figure 4:** Different diffraction regimes depending on the Fresnel number  $F_0$ . The parameters  $a$  and  $b$  refer to the diameter of the scattering object and the length of the area over which the scattering objects are distributed, respectively. In the contact region ( $F_0 = \infty$ ) the object is still visible, purely based on absorption. In the Fresnel regime ( $F_0 \approx 1$ ) fringes at the edges become visible due to interference. In the Fraunhofer regime ( $F_0 \ll 1$ ) only the diffraction pattern can be seen with the phase information encoded in it [6].

If  $F_0 \rightarrow \infty$  one is in the contact region and only the absorption contrast is visible. With increasing propagation distance, more and more fringes become visible. If  $F_0 \approx 1$  one talks about Fresnel diffraction in the near-field, where the absorption contrast, but also some fringes resulting from the phase contrast are visible. These fringes, caused by the interference of the refracted and diffracted waves, enhance the edges of features in the sample.  $F_0 \ll 1$  refers to Fraunhofer diffraction in the far-field. Here, only the diffraction pattern can be seen. The experiment at the synchrotron in this thesis was performed in the Fresnel diffraction regime [6].

In order to make the phase shift, and hence phase contrast, visible, it would be easiest if the phase could be directly measured. However, a direct detection is impossible because no detector can measure the fast frequencies of  $\sim 10^{15}$  Hz of electromagnetic waves. Only the intensities can be detected, which is enough to retrieve phase information and recover the original object as will be explained in Section 3.3.1 [12].

For measuring phase contrast, the so called propagation based imaging can be used, where the freely propagating beam is detected. One possibility to retrieve the phase information is to measure the deflection of the waves. That means that the beam is detected without a sample first, followed by a measurement with sample. The detected intensities show the deflection and, as shown in Equation (5) and (6), this is proportional to the change in phase, which in turn is proportional to the change in  $\delta$ . The varying values of  $\delta$  can then be used to build up an image [5].

The method for phase retrieval that was used in this thesis is based on the assumption of having a thin and homogeneous sample, meaning that  $\delta$  is constant. In that case, the *Paganin* algorithm [13], which is based on the transport-of-intensity equation (TIE) and will be introduced in Section 3.3.1, can be used to reconstruct the original object.

To conclude this section, the advantages of phase contrast imaging based on free-space propagation are listed: This freely propagating method does not require the use of lenses, so no aberrations can be induced by them. Applying phase contrast delivers the possibility to distinguish easier between different features of a sample because of a better contrast

(edge enhancement), which is also the case for materials with similar absorption properties such as biological tissue. Lastly, the radiation dose and hence radiation damage can be decreased, as was pointed out earlier [13].

### 2.1.3 Resolution and Dose

The radiation dose  $D$  has the unit Gray (Gy) and is the deposited energy per mass [11]. In order to detect a signal in imaging, one needs a minimum required surface dose, shown in Equation (8) [14].

$$D = \frac{\mu N_0 h\nu}{\epsilon} \propto d^{-4} \quad (8)$$

The parameters  $\mu$ ,  $N_0$ ,  $h\nu$ ,  $\epsilon$  and  $d$  are defined as the absorption coefficient, incident number of photons per unit area, photon energy, density of the material and resolution [14].

From Equation (8) it can be learnt that  $D$  scales as  $d^{-4}$ , i.e. a higher dose leads to a better resolution. Therefore, in order to achieve a higher resolution by increasing the dose, a higher number of incident photons per unit area  $N_0$  on the sample is needed. This can be fulfilled by either increasing the exposure time or by having a higher fluence [11, 15]. In addition, one should be able to distinguish between signal and noise in an image. Thus, the signal-to-noise ratio (SNR) has to be considered. As the SNR depends on the number of incident photons per unit area, a higher SNR leads to the need of a higher dose. It was found that a SNR of five is sufficient to distinguish between signal and noise. This requirement on the SNR is called Rose criterion [14].

On the other side, a higher dose leads to radiation damage, meaning the breaking of chemical bonds due to irradiation and possible subsequent reaction of the sample's fragments as a consequence. The occurrence of radiation damage is the major limitation when it comes to X-ray imaging of biological samples. Consequently, there is a maximum tolerable dose that should not be exceeded in order to avoid radiation damage when performing such experiments. The required and maximum tolerable dose for a protein are illustrated in Figure 5 [14, 16].

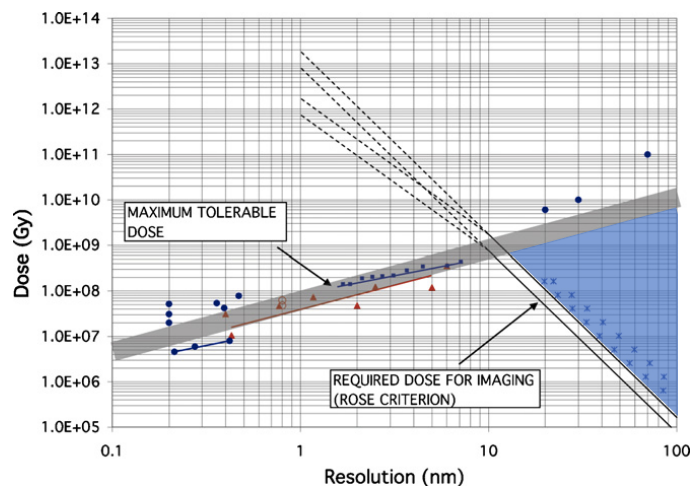


**Figure 5:** Required and maximum tolerable dose for a protein ( $\text{H}_{50}\text{C}_{30}\text{N}_9\text{O}_{10}\text{S}_1$ ) as a function of resolution (nm) with water as background. The lower line (higher line) refers to an X-ray energy of 1 keV (10 keV). The blue triangle shows the area that is suitable for imaging experiments [14].



Here, the dependency between dose and resolution is illustrated. In principle, a higher dose leads to a better resolution, as can be seen by the line of the required dose for imaging. However, this comes with the cost of inducing and increasing radiation damage, requiring the need to stay below the maximum tolerable dose. Therefore, only the right triangle (blue) with an overlap between maximum tolerable dose and required dose is suitable for imaging [14].

As stated earlier, the limitation given by radiation damage can be drastically improved by looking at phase contrast, as the absorption process becomes less dominant at higher photon energies (hard X-rays). These phase contrast techniques are also known as coherent imaging techniques. As the name suggests, their implementation requires using coherent X-rays, whose generation is described in Section 2.1.4 [11].

#### 2.1.4 X-Ray Sources

To understand the requirement of a coherent beam, the term "coherence" is defined first. In short, coherence describes the phase relation between two waves. Here, it has to be distinguished between temporal and spatial coherence. Temporal coherence describes the property of two waves having the same phase at two different times. The higher the monochromaticity of the beam, the more time it takes for the waves to get out of phase. In case of spatial coherence, the waves are assumed to have the same wavelength, but slightly different propagation directions. This is determined by the size of the source and divergence of the beam. Spatial coherence describes the two waves having the same phase at two different locations in space (independent of time) [17].

For phase contrast imaging, spatial coherence is of importance. That is because the fringes created by the interference between the waves that pass through the sample and those that do not (i.e. reference waves) are only clearly visible when the source size is small enough [6].

A measure for the coherence of the beam is given by its brightness  $B$ . This is defined as follows (Equation (9)) [17]:

$$B = \frac{\text{photons/s}}{\text{mm}^2 \text{ mrad}^2 0.1 \% \text{ BW}} \quad (9)$$

That means that the higher the brightness, the higher the coherence. The brightness for different kinds of X-rays sources is shown in Figure 6 [18]. The brightness of synchrotron light sources using undulators, which consist of several magnets, is approximately 10 orders of magnitudes greater than that provided by X-ray tubes in a laboratory.

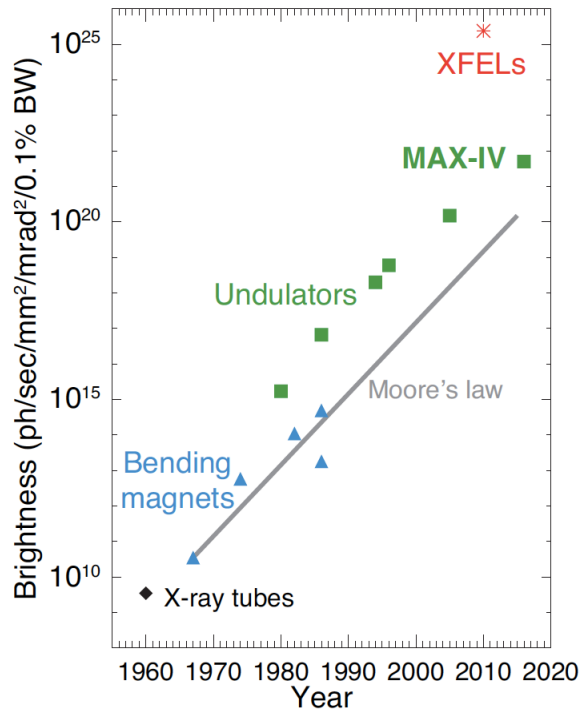


**Figure 6:** Brightness for different X-ray sources and their historical development from 1960 to 2020 [18].

The easiest and oldest way to generate X-rays is to use laboratory X-ray sources. An example of a laboratory X-ray source is shown in Figure 7, where a cathode filament is heated to a temperature that is high enough to overcome the electrons' work function energy and hence free some of the electrons. Subsequently, the electrons are accelerated towards an anode and hit a metal target (tungsten). Most of the converted energy is transferred into heat. However, bremsstrahlung and characteristic X-rays are created, too [18, 19].

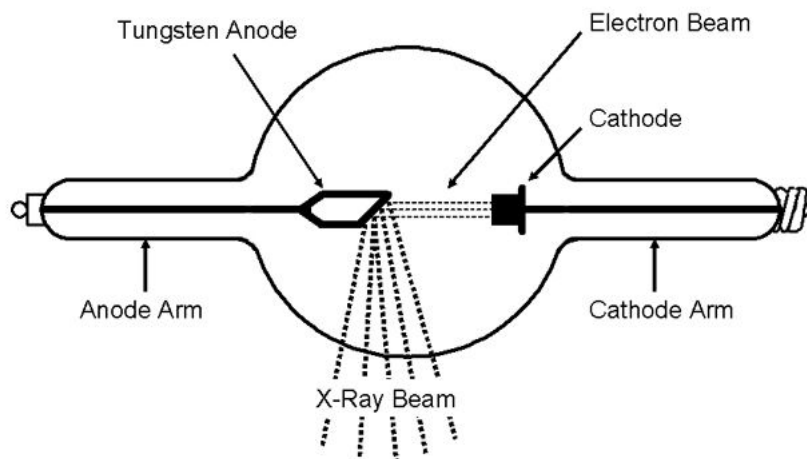


**Figure 7:** Generation of X-rays using a laboratory X-ray source. Electrons are freed from a cathode by heating and accelerated towards an anode. They hit a tungsten target, leading to the creation of X-rays [19].

Another source that generates X-rays is a synchrotron light source. The typical construction of a synchrotron is illustrated in Figure 8 [17]. Electrons are generated by an electron gun (in a similar way as described for the laboratory X-ray source). These electrons are then accelerated by a linear accelerator (LINAC) and injected into a booster ring, where further acceleration takes place. When they reach the energy of the electrons in the storage ring (velocity close to the speed of light), they are injected into it and kept at a constant energy [17].

In the curved sections of the storage rings the so called bend achromats are placed. They consist of dipole, quadrupole and sextupole magnets. The dipoles deflect the electrons in order to maintain their path. The quadrupoles focus the electron beam and the sextupoles take care of correcting chromatic aberrations [17]. The insertion devices (IDs) are positioned in the straight sections of the storage rings. This is where the synchrotron radiation is created. The IDs contain several dipoles with alternating magnetic field orientations. This causes the electrons to be deflected up and down several times, leading to the generation of synchrotron radiation. Depending on how much the electrons are deflected from their original path, one distinguishes between wigglers and undulators. In wigglers the electrons deviate from their path in a way that the produced radiation does not interfere, i.e. the angular excursion is large compared to the one from undulators. In undulators, the deviation of the electrons is smaller, leading to an interference of the radiation. The consequence is that the produced radiation has different characteristics. The spectrum of radiation generated by wigglers is continuous and of lower brightness compared to that of undulators. The reason for the undulator spectrum being discrete and reaching higher brightness values is given by the interference that was mentioned before [17].

Due to the generation of synchrotron radiation, an energy loss of the electron beam takes place. In order to keep the beam at a constant energy, a radio frequency (RF) cavity is used. Whenever the electrons pass through the cavity, they will either be accelerated or decelerated, depending on their velocity. This leads to the formation of bunches [17].

Since the generated synchrotron radiation is uncharged, it is not influenced by the bending magnets and leaves the storage ring by entering the beamline. A beamline consists of an optical hutch, where the X-rays' temporal and phase-space properties are modified, and experimental hutch [17].

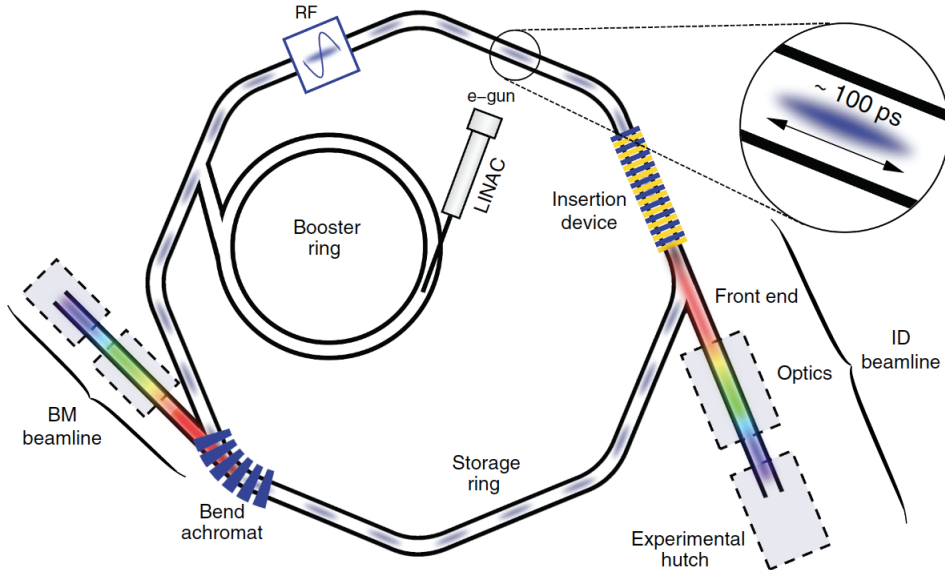


**Figure 8:** The design of a synchrotron, including an electron gun, LINAC, booster ring, storage ring, RF cavity, insertion device, magnets and beamline with optical and experimental hutches [17].

As soon as the X-rays are generated, the actual experiments can be performed, as described in Section 2.2.

## 2.2 Tomography

As discussed earlier, X-rays are of non-destructive and deeply penetrating nature. This is advantageous when it comes to tomography, where 3D images of samples are recorded. Tomography is originally a Greek word consisting of "tomos" ("to slice") and "graph" ("image"). The main idea is to get 2D images of many slices of the sample and put these images together afterwards to obtain a 3D image. Thus, this technique makes it possible to visualize the internal structures of the sample's volume in a non-destructive manner. An exemplary working principle of tomography is shown in Figure 9 [6].

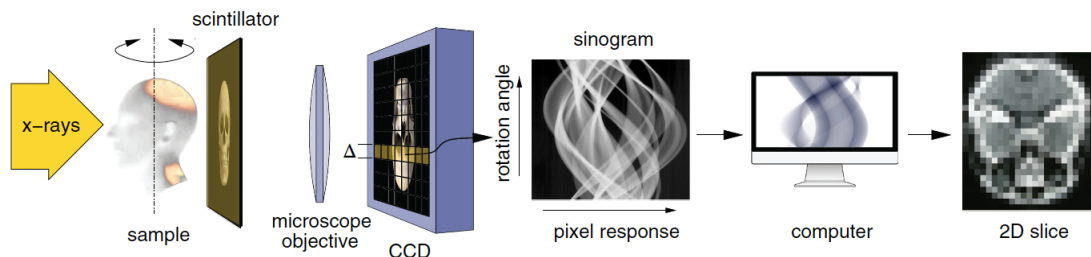


**Figure 9:** Working principle of tomography. X-rays are used to illuminate a sample, which is rotated. The transmitted X-rays are converted to visible light by a scintillator and the signal is magnified by a microscope objective afterwards. The signal is detected by a CCD camera, where one row of pixels corresponds to one slice of the sample. For each slice a sinogram is generated, which is used to reconstruct the 2D slice [6].

In the example of Figure 9, a sample is illuminated with X-rays and the transmitted photons hit a scintillator, where they are converted into visible light. This signal is then magnified by a microscope objective and detected by a CCD camera afterwards. Each pixel row on the CCD camera corresponds to one slice of the sample (i.e. the resolution is limited by the pixel size). As the sample is rotated during this procedure, signals at several angles are obtained. The angles range from  $0^\circ$  to  $180^\circ$ . This is enough to reconstruct the overall sample in the end, as the angles ranging from  $181^\circ$  to  $360^\circ$  contain the same information, just the other way around [6, 20].

The detected projections at all angles are used to generate the so called sinogram. Projection means here the line integral along the propagation direction for each pixel, i.e. the summed up intensities. Mathematically the projection is described by the Radon transform, which is a function of the position at the detector and angle [5], and the interested reader is referred to [21] to find out more about it. The sinogram displays the detected intensities for all pixels/detector positions of one slice for the different rotation angles. Its name originates from the fact that features within a sample follow a sinusoidal shape when the sample is rotated. Since the sinogram contains the information of the projections, it can then be used to generate the image of one slice [5].

In order to determine the needed size of each rotation step and hence the number of projections  $N_\theta$ , the Crowther criterion can be applied. It is described by Equation (10) for the case of a  $180^\circ$  measurement with the number of the slice's pixels  $N_{x'}$  (in case of  $360^\circ$   $N_{x'}$  is only multiplied with  $\pi$ ) [21]:

$$N_\theta = \frac{\pi}{2} N_{x'} \quad (10)$$

There are several approaches that can be used to reconstruct the individual slices, one of them being introduced in Section 2.2.2. All slices can then be combined afterwards to obtain the whole 3D image. In order to understand the reconstruction process, the Fourier slice theorem is introduced first in Section 2.2.1.

### 2.2.1 Fourier Slice Theorem

The approach that was used for the image reconstruction in this thesis is based on the Fourier slice theorem. It can be understood in the following way: One slice of the sample is described by a 2D function  $f(x, y)$  with its Fourier transform (FT)  $F(q_x, q_y)$  (Equation (11)).

$$F(q_x, q_y) = \int \int f(x, y) e^{i(q_x x + q_y y)} dx dy \quad (11)$$

When considering one slice through the FT ( $q_y = 0$ ), this leads to:

$$F(q_x, q_y = 0) = \int \left[ \int f(x, y) dy \right] e^{iq_x x} dx \quad (12)$$

When one looks at one projection, i.e. integrates  $f(x, y)$  along the y-axis, the resulting function  $p(x)$  of the projection only depends on one coordinate (see Equation (13)).

$$p(x) = \int f(x, y) dy \quad (13)$$

With applying the FT to  $p(x)$ , one gets:

$$P(q_x) = \int p(x)e^{iq_x x} dx \quad (14)$$

The Equations (11) to (14) can be combined to obtain:

$$F(q_x, q_y = 0) = \int p(x)e^{iq_x x} dx = P(q_x) \quad (15)$$

From Equation (15) it can be learnt that one slice through the FT of the original function  $f(x, y)$  equals the FT of one projection  $p(x)$  [5, 21].

### 2.2.2 Filtered Backprojection

The filtered backprojection (FBP) is a method for image reconstruction that is based on the Fourier slice theorem. The idea is to combine all the FTs  $P(q_x)$  of the individual projections of one slice (at all angles) to form the FT  $F(q_x, q_y)$  of the overall slice. By applying the inverse FT afterwards, the slice  $f(x, y)$  can be reconstructed. However, before applying the inverse FT, there are several factors that need to be considered:

1. Different amount of information at different frequencies. At low frequencies, there is a higher overlap of the projections' information.
2. Noise at higher spatial frequencies.
3. Regridding from the polar grid (Fourier space) to the Cartesian coordinate system (spatial domain).

In order to take into account 1, the data has to be weighted before the inverse FT, which is done by applying a filter that suppresses lower frequencies. Additional filters can be applied to suppress higher frequency noise to compensate for 2. The regridding process 3 can be performed by simple interpolation, which can introduce non-negligible errors, or, more commonly, by convolving the FTs of the individual slices with the FT of a specific window function  $W(x, y)$ . Afterwards, the inverse FT is applied and the contribution of  $W(x, y)$  is removed by dividing the obtained image by  $W(x, y)$  [21]. This overall procedure can be performed by the so called *gridrec* algorithm [22].

### 2.2.3 Corrections

When the transmitted photons are detected by the detector, one has to consider two factors: The inherent noise of the detector's electronics and a not perfectly homogeneous beam. To correct the former, a dark image is recorded first, where sample and beam are absent. For the latter, one records the flat-field, i.e. the beam is turned on, but the sample is removed from the beam. The intensities of these signals have to be taken into account to get rid of varying detector responses by performing the flat-field correction (Equation (16)) [6, 23].

$$I_{\text{normalized}} = \frac{I_{\text{raw}} - I_{\text{dark}}}{I_{\text{flat}} - I_{\text{dark}}} \quad (16)$$

Here,  $I_{\text{normalized}}$ ,  $I_{\text{raw}}$ ,  $I_{\text{dark}}$  and  $I_{\text{flat}}$  refer to the intensities of the normalized data, raw data, dark and flat-field, respectively.

## 3 Methods

X-ray tomography was performed on samples of the bowel at a micro-CT setup in Lund in Sweden and at the TOMCAT beamline of the synchrotron at the Paul-Scherrer-Institut (PSI) in Switzerland. The obtained images were based on absorption or phase contrast. For the latter, the phase information was retrieved for all projections to generate the sinograms, following the procedure described in Section 2.2.

### 3.1 Sample

The studied samples were tissue of the bowel (colon and/or ileum) of patients of different ages and genders. Control samples of healthy patients were investigated, too. All data has been made anonymous and the studies were conducted with consent of the patients. The samples were obtained by surgery and embedded in paraffin. In this thesis, the sample of one diseased patient was studied particularly.

### 3.2 Data Acquisition

This section presents the process of data acquisition. For this purpose, the setups are introduced first, followed by the used parameters. The details about the micro-CT and synchrotron experiment are described in Section 3.2.1 and Section 3.2.2, respectively.

#### 3.2.1 Micro-CT

One setup that was used for the investigation of the samples is a micro-CT (Figure 10). The X-rays are generated by an Excillum prototype tungsten anode microfocus X-ray source and illuminate the sample. The transmitted and refracted photons are detected by a DECTRIS EIGER2 R 500K detector [24], which is a single photon counting detector [25]. This type of detector works by having a sensor material (here silicon), in which electrical charges are created when the X-rays impinge on it. The charges move towards an electrode due to the presence of an electric field and induce a signal that is proportional to the number of photons and their energy [26].

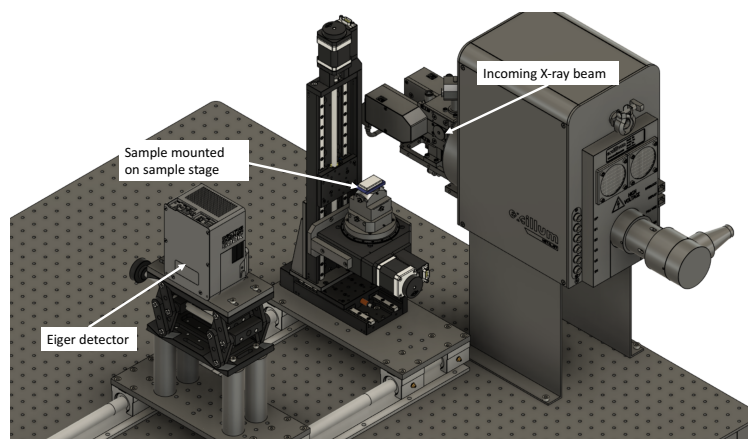


**Figure 10:** The overall experimental setup of the micro-CT. The X-rays are generated by an Excillum lab based source and illuminate the sample. The refracted and transmitted photons are detected by the EIGER detector [27].

The parameters of the setup are listed in Table 1. A scan with  $4 \times$  magnification was performed. The magnification was chosen by adapting the source-sample and source-detector distance.

**Table 1:** Used parameters at the micro-CT setup.

Photon energy	polychromatic bremsstrahlung with 70 kV acceleration voltage and tungsten target
Effective photon energy [keV]	14.035
Beam geometry	cone
Physical pixel size [ $\mu\text{m}$ ]	75
Effective pixel size [ $\mu\text{m}$ ]	18.75
Number of projections	2000
Recorded angles [degrees]	0-360
Source-sample distance [m]	0.25
Source-detector distance [m]	1
Field of view (FoV) [pixels]	$1028 \times 512$
Exposure time [s]	10

### 3.2.2 TOMCAT Beamline

The samples were also examined at TOMCAT, which is a beamline at the Swiss Light Source (SLS). It delivers a photon flux in the order of  $10^{14}$  photons/s, a photon source size of  $140 \mu\text{m}$  (horizontally)  $\times$   $45 \mu\text{m}$  (vertically) and a photon source divergence of 2 mrad (horizontally)  $\times$  0.6 mrad (vertically). The energy of the beam is selected by a double crystal multilayer monochromator and ranges from 8 to 45 keV with a bandwidth in the order of  $10^{-2}$  [20].

The experimental station is shown in Figure 11. The sample is positioned in the desired way by moving the sample stage and irradiated by the incoming X-ray beam (left). The transmitted and refracted photons are then detected by the detector system [20].

In comparison to the micro-CT system, the detector here consists of a scintillator, optical microscope and visible light camera (right). The scintillator converts the X-rays to visible light. Afterwards, the light is deflected by a mirror onto an optical microscope, where the image is magnified. Different optical magnifications (i.e. different optical microscopes) are available at TOMCAT. Finally, the image is detected by a scientific CMOS camera [20].



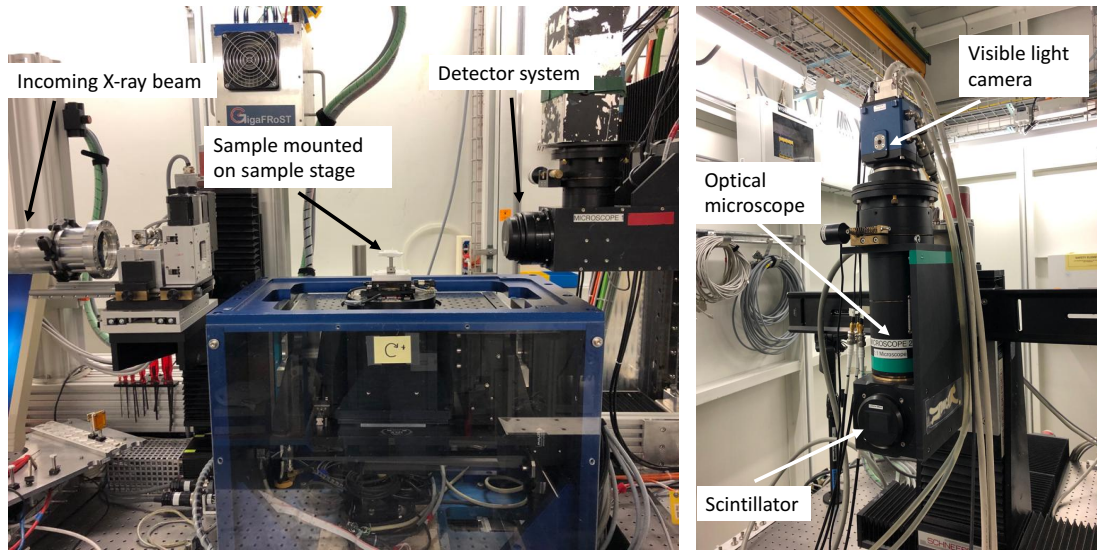


**Figure 11:** The overall experimental setup at TOMCAT (left) and the components of the detector system (right). The sample can be positioned precisely by moving the sample stage and is illuminated with X-rays. The transmitted and refracted photons are then converted into visible light. The signal is magnified by an optical microscope and detected by a camera.

The tomographic measurements were performed in different stages. First, a low-resolution 3D image ( $1 \times$  magnification) was recorded for each sample. This overview scan was used to determine the regions with the ENS. In most cases, the regions of interest (ROIs) could be identified just by looking at the absorption contrast images. This is advantageous as the phase retrieval takes additional time. However, sometimes additional phase retrieval was performed to resolve more details and be able to select the ROIs. Afterwards, high-resolution 3D images ( $4 \times$  magnification) of the ROIs were recorded and phase retrieval was performed on all of them. The final results were 3D images of the ROIs with high resolution and phase contrast.

The parameters of the low- and high-resolution scans are listed in Table 2. The reason for taking projections at the rotation angles ranging from  $0^\circ$  to  $360^\circ$  in the case of low resolution is given by the possibility that the sample might not be completely covered by the beam. Hence, it can only be ensured to catch all features of the sample when it is rotated by  $360^\circ$ .

For the high-resolution images, a smaller region (ROI) is selected and positioned precisely in a way that it is completely covered by the beam, i.e. a coverage of  $180^\circ$  is sufficient.

**Table 2:** Used parameters for low- and high-resolution scans.

	Low resolution	High resolution
Photon energy [keV]	21 (monochromatic)	21 (monochromatic)
Beam geometry	parallel	parallel
Scintillator	LuAg:Ce 300 $\mu\text{m}$	LuAg:Ce 20 $\mu\text{m}$
Pixel size [ $\mu\text{m}$ ]	6.5 (physical)	1.625 (effective)
Number of projections	5001	1801
Recorded angles [degrees]	0-360	0-180
Sample-detector distance $z$ [m]	3	0.19
FoV [pixels]	2040 $\times$ 590	2560 $\times$ 2160
Exposure time [s]	0.02	0.08

Choosing a high spatial resolution always involves some trade-offs. In general, the resolution  $\delta_r$  depends on the wavelength  $\lambda$  and numerical aperture (NA) and is defined as [11]:

$$\delta_r = 0.61 \frac{\lambda}{\text{NA}} \quad (17)$$

With  $\text{NA} = 0.16$  [20] and the LuAg:CE 20  $\mu\text{m}$  emitting light with a wavelength of about 535 nm [28] in case of the 4  $\times$  magnification, this leads to:

$$\delta_r = 0.61 \frac{535 \text{ nm}}{0.16} \approx 2 \mu\text{m} \quad (18)$$

However, in the end the pixel size is the limiting factor, which is 1.625  $\mu\text{m}$  as can be seen in Table 2. According to [20], not one, but about three pixels are required to identify a feature in the sample, leading to a resolution of 4.875  $\mu\text{m}$ .

Additional aspects that have to be considered when it comes to resolution and focusing the image onto the detector plane are the depth of focus DOF and thickness of the scintillator. These two quantities have to match, i.e. the scintillator thickness has to be equal or smaller than the DOF. If this requirement is not fulfilled, points that do not lay on the focal plane of the lens within the scintillator will produce an unfocused image that will hinder the resolution. Consequently, a thin scintillator is desirable for high-resolution imaging. At the same time, the downside of thinner scintillators is that they tend to have lower light yield if their thickness is smaller than the attenuation length [20, 29].

As has already been mentioned previously, the experiments were performed in the near-field regime. To prove this vividly, the Fresnel number for the high-resolution setup is calculated in the following by using Equation (7). The size of a scattering object/ feature is assumed to be  $a = 3 \cdot 1.625 \mu\text{m} = 4.875 \mu\text{m}$  because three pixels are needed to resolve a feature, as described above. As can be seen in Table 2,  $z = 0.19 \text{ m}$  and  $E = 21 \text{ keV}$  ( $\lambda = hc/E = 5.9 \cdot 10^{-11} \text{ m}$  with Planck constant  $h$  [30]).

$$F_0 = \frac{(4.875 \cdot 10^{-6} \text{ m})^2}{0.19 \text{ m} \cdot 5.9 \cdot 10^{-11} \text{ m}} \approx 2.12 \quad (19)$$

With this,  $F_0$  is close to the expected order of magnitude of  $F_0 \sim 1$ .

### 3.3 Data Analysis

This section describes the processing of the recorded data. First, the algorithm used for phase retrieval is introduced in detail (Section 3.3.1). This is followed by the tomographic reconstructions of the data obtained by the micro-CT and TOMCAT in Section 3.3.2 and 3.3.3.

#### 3.3.1 Phase Retrieval with TIE

For the phase retrieval and reconstruction of the original object, the algorithm developed by Paganin et al. [13] was applied and implemented using the pyPhase Python package [31]. This approach is based on the TIE (Equation (20)), which describes the progression of the intensity of an electromagnetic wave as it propagates and correlates the wave's intensity  $I(\mathbf{r}_\perp, z)$  with its phase  $\varphi(\mathbf{r}_\perp, z)$ . The optic axis  $z$  points in the direction of propagation and the position vector  $\mathbf{r}_\perp$  is perpendicular to it [13].

$$\nabla_\perp \cdot (I(\mathbf{r}_\perp, z) \nabla_\perp \varphi(\mathbf{r}_\perp, z)) = -\frac{2\pi}{\lambda} \frac{\partial}{\partial z} I(\mathbf{r}_\perp, z) \quad (20)$$

When being in the contact region ( $z = 0$ ), as described in Section 2.1.2, the absorption contrast is dominant and thus the Beer-Lambert law (Equation (2)) holds. Therefore, the intensity can be written as:

$$I(\mathbf{r}_\perp, z = 0) = I_0 \cdot \exp(-\mu T(\mathbf{r}_\perp)) \quad (21)$$

with the object thickness  $T(\mathbf{r}_\perp)$ . Assuming a single material, this thickness can also be related to the phase via:

$$\varphi(\mathbf{r}_\perp, z = 0) = -\frac{2\pi}{\lambda} \delta T(\mathbf{r}_\perp) \quad (22)$$

with the refractive-index decrement  $\delta$  as defined in Section 2.1.1. That means that the phase information is encoded in the sample's thickness as the ratio  $\delta/\beta$  is unique for each material. By substituting Equation (21) and Equation (22) into Equation (20), rearranging and applying FTs to the intensities in the contact region ( $z = 0$ ) and at a specific distance  $R$  ( $z = R$ ), one obtains the expression:

$$T(\mathbf{r}_\perp) = -\frac{1}{\mu} \ln \left( F^{-1} \left\{ \mu \frac{F\{I(\mathbf{r}_\perp, z = R)\}/I_0}{R\delta|\mathbf{k}_\perp|^2 + \mu} \right\} \right) \quad (23)$$

with the wave vector  $\mathbf{k}_\perp$ . The detailed derivation of this expression is omitted here, however, it can be found in [13]. With Equation (3), (22) and (23), one obtains the final equation for the retrieved phase:

$$\varphi(\mathbf{r}_\perp) = \frac{\delta}{2\beta} \ln \left( F^{-1} \left\{ \frac{F\{I(\mathbf{r}_\perp, z = R)\}/I_0}{1 + \frac{\lambda R \delta}{4\pi\beta} |\mathbf{k}_\perp|^2} \right\} \right) \quad (24)$$

That means, that the phase information can be retrieved by measuring the intensities. The additional parameters that have to be set to apply the *Paganin* algorithm are the wave vector (by setting the energy), propagation distance and  $\delta/\beta$  ratio, as can be seen in Equation (24). The energy and propagation distance are determined by the experimental setup. In case of a polychromatic X-ray source, the setups' effective energy (see Table 1) has to be used. By varying the  $\delta/\beta$  ratio, the phase can be influenced. From Equation (24) it becomes apparent that the *Paganin* algorithm acts as a low-pass filter: High-frequency

noise is reduced and depending on the  $\delta/\beta$  ratio this effect is more or less pronounced, i.e. increasing the  $\delta/\beta$  ratio reduces high-frequency noise more. However, this filtering comes with the cost of losing information, hence decreasing the resolution.

### 3.3.2 3D Image Reconstruction of Micro-CT Data

For the image reconstruction of the micro-CT data, the procedure described in Section 2.2.2 was applied. However, the used algorithm was the *FDK* algorithm [32], which takes into account the cone geometry of the beam (in contrast to the parallel beam geometry in case of the *gridrec* algorithm). The ramp filter [33] was used for the suppression of lower frequencies, as described in Section 2.2.2.

A problem that occurred during the micro-CT measurements was the presence of ring artifacts in the reconstructed images. Ring artifacts are caused by defective or miscalibrated detector elements. Incorrect pixel responses lead to the occurrence of vertical or horizontal stripes in the sinograms. As a consequence, bright rings are visible in the reconstructed images, hence decreasing the image quality. In order to overcome this, a wavelet-fast FT filter [34] was used, which eliminates the stripes from the very beginning.

### 3.3.3 3D Image Reconstruction of TOMCAT Data

For the 3D image reconstruction of the TOMCAT data, the *gridrec* algorithm explained in Section 2.2.2 was used. This was done with the TomoPy Python package [23]. In order to reduce noise, a filter, as mentioned in Section 2.2.2, was applied. This low-pass *Parzen* window was used in order to filter out high-frequency noise [33].

Combining all the information given above, the overall procedure can be described as follows:

1. Measure intensities (= projections) of transmitted and refracted beam for each slice at different angles.
2. Optional: Perform phase retrieval with *Paganin* on projections to get phase information and compute corresponding sinograms. Otherwise proceed with sinograms that are based on absorption contrast.
3. Reconstruct 2D slices by applying the FT to the projections and combining all individual FTs to one FT of the whole slice. In the Fourier space, filtering operations are performed and regridding takes place. Afterwards, an inverse FT is applied. Overall, this is done by:
  - (a) applying the *FDK* algorithm for micro-CT data
  - (b) applying the *gridrec* algorithm for synchrotron data.
4. Combine all 2D slices to get 3D volume.

As soon as the images are reconstructed, they can be segmented into their components for further analysis, as described in Section 3.4.

### 3.4 Image Segmentation

Image segmentation describes the procedure of dividing an image into several segments with similar properties (e.g. shape). In order to do this, ROIs are created, in which labels are assigned to the voxels of the image. Using the labels and original dataset, parameters of the individual segments (e.g. volume) can be extracted. For the image segmentation in this thesis, it was worked with *Dragonfly* [35], a software for image processing.

In order to distinguish between different components of the images, here between background and cells in the foreground, the *Otsu* algorithm [36] was used for the threshold selection as a starting point and if necessary a manual adjustment was made. The *Otsu* method can be applied for gray-level images and makes it possible to separate foreground (higher intensity pixels) from background (lower intensity pixels) by looking at the image histogram. In order to find the threshold that defines the cut between fore- and background, the following approach is used: One starts by defining the probability  $p_i$  of finding a pixel with a specific gray level  $i$  as shown in Equation (25).

$$p_i = \frac{n_i}{N} \quad (25)$$

Here,  $n_i$  and  $N$  are defined as the number of pixels with the gray level  $i$  and total number of pixels, respectively. Next, it is distinguished between back- and foreground by defining two classes  $C_0$  and  $C_1$  with the gray values ranging from 1 to the threshold  $k$  for the former and from  $k + 1$  to the maximum gray value  $L$  for the latter. The corresponding probability distributions are:

$$\omega_0 = \Pr(C_0) = \sum_{i=1}^k p_i \quad (26)$$

and

$$\omega_1 = \Pr(C_1) = \sum_{i=k+1}^L p_i \quad (27)$$

The means are defined as:

$$\mu_0 = \sum_{i=1}^k i \Pr(i|C_0) = \sum_{i=1}^k \frac{i p_i}{\omega_0} \quad (28)$$

and

$$\mu_1 = \sum_{i=k+1}^L i \Pr(i|C_1) = \sum_{i=k+1}^L \frac{i p_i}{\omega_1} \quad (29)$$

This leads to the variances:

$$\sigma_0^2 = \sum_{i=1}^k (i - \mu_0)^2 \Pr(i|C_0) = \sum_{i=1}^k (i - \mu_0)^2 \frac{p_i}{\omega_0} \quad (30)$$

and

$$\sigma_1^2 = \sum_{i=k+1}^L (i - \mu_1)^2 \Pr(i|C_1) = \sum_{i=k+1}^L (i - \mu_1)^2 \frac{p_i}{\omega_1} \quad (31)$$

As a next step, it can be distinguished between the within-class variance  $\sigma_W^2$ , the between-class variance  $\sigma_B^2$  and the total variance  $\sigma_T^2$ :

$$\sigma_W^2 = \omega_0\sigma_0^2 + \omega_1\sigma_1^2 \quad (32)$$

$$\sigma_B^2 = \omega_0(\mu_0 - \mu_T)^2 + \omega_1(\mu_1 - \mu_T)^2 \quad (33)$$

$$\sigma_T^2 = \sigma_B^2 + \sigma_W^2 \quad (34)$$

Here,  $\mu_T = \omega_0\mu_0 + \omega_1\mu_1$  is the total mean. The optimum threshold  $k$  is found when  $\sigma_B$  is maximized (and  $\sigma_W$  is minimized) [36, 37].

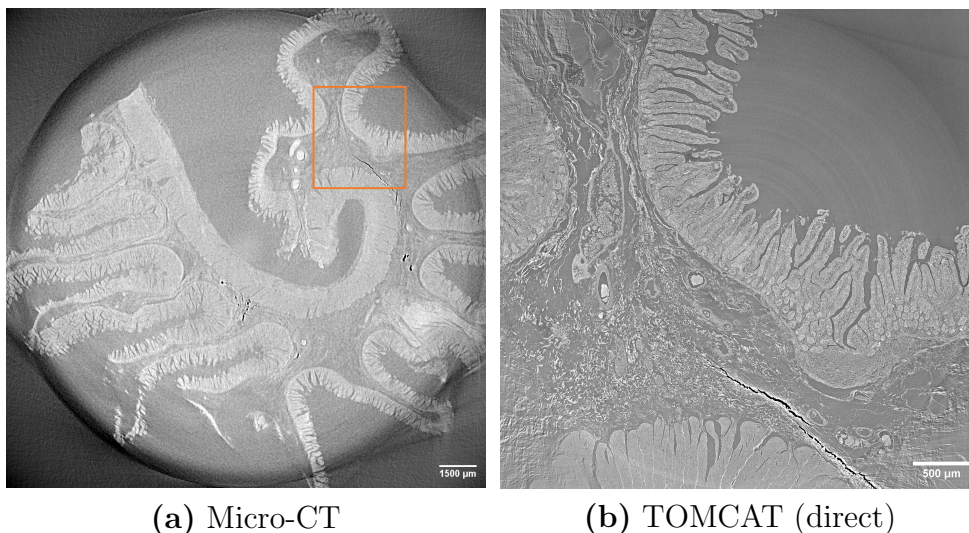
Once the image is divided into fore- and background, the properties of the individual components, here mean intensities and volume, can be determined.

## 4 Results

This section presents the results of this master thesis. It is started by showing the overall reconstructed 2D images of an intestinal sample with their corresponding histograms of a chosen slice for the two different setups in Section 4.1. In general, the reconstruction of the data acquired by the TOMCAT setup is divided into direct and self-developed, hereafter referred to as SD, reconstruction. The direct reconstruction refers to the reconstruction procedure performed at the beamline, whereas the SD reconstruction means obtaining the reconstructed images by using the Python scripts that can be found in the Appendix. This is followed by the comparison of the setups' CNR and evaluation of the setups in terms of resolving the ganglia, that are made up of neurons as described in Section 1, in Section 4.2. Afterwards, the focus is shifted towards the phase contrast, including an approach for its improvement in case of the lab based source in Section 4.3. As a final result, an optimal segmentation of ganglia of one sample is shown in Section 4.4.

### 4.1 Image Reconstructions of Selected Slices

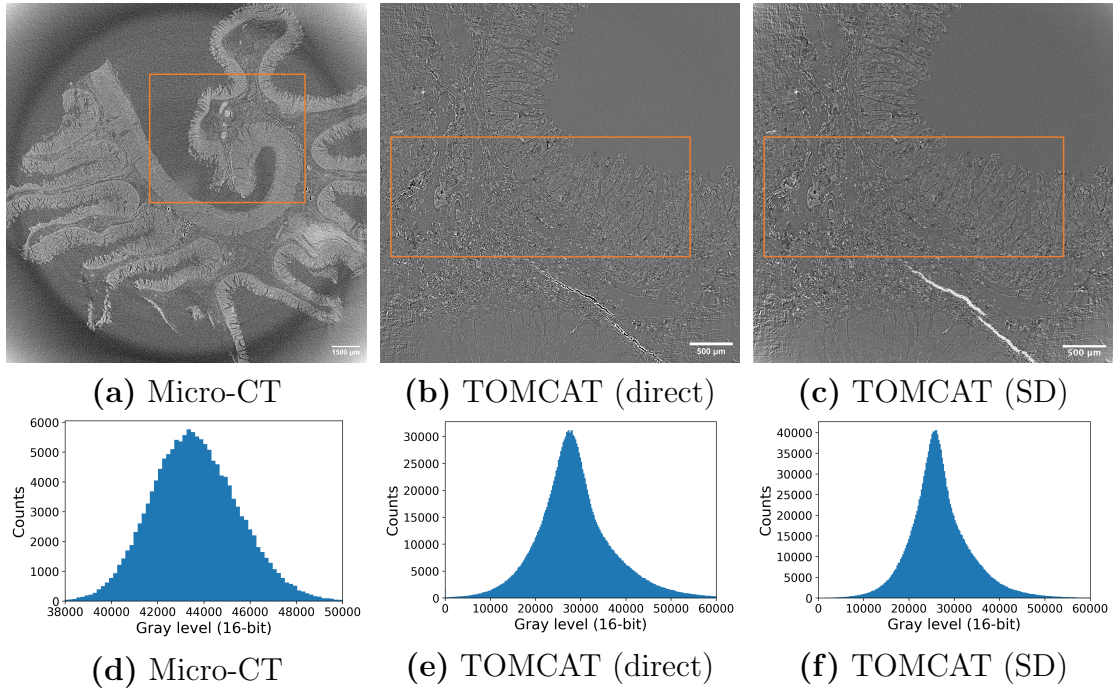
An overview of the investigated sample is given in Figure 12. The FoV in Figure 12(a) covers the complete sample and the image was recorded with the micro-CT and a  $4 \times$  magnification. The FoV of the  $4 \times$  magnification images recorded by the TOMCAT setup (Figure 12(b)) covers only part of the sample, more specifically the part that is marked by the orange box in Figure 12(a).



**Figure 12:** Reconstructed images ( $4 \times$  magnification) with phase retrieval. The orange box in (a) is the part of the sample that is covered by the FoV in (b).

The reconstructed images and corresponding histograms obtained by algorithms without phase retrieval are illustrated in Figure 13. The reconstructions were performed either directly at the experimental station (Figure 13(a) and (b)) or with SD scripts for the TOMCAT data (Figure 13(c)). The orange boxes mark the regions that were used to obtain the histograms that are shown in Figure 13(d), (e) and (f). The histograms show how the pixels with different gray level values are distributed. All three histograms show one peak and especially Figure 13(e) and (f), where the same dataset was used, have similar distributions in terms of gray level range and distribution shape. When compar-

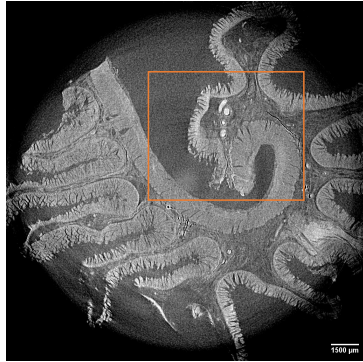
ing Figure 13(b) with (c), it can be seen that the edges of the image in (c) are slightly brighter.



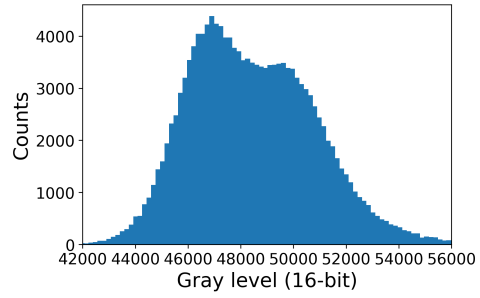
**Figure 13:** Reconstructed images ( $4 \times$  magnification) and corresponding histograms without phase retrieval. The TOMCAT data was additionally reconstructed using SD Python scripts. The orange boxes show the regions that were used to create the histograms.

Figure 14 shows equivalent results to Figure 13 with the difference that phase retrieval was used. Here, it is especially noticeable that the histograms show two peaks: One more pronounced peak at lower gray level values, and one less pronounced one at higher gray level values. In Figure 14(a)-(e) the same  $\delta/\beta$  ratio was used (optimized value from TOMCAT beamline: 217.6). However, Figure 14(d) and (f) differ despite the fact that the same dataset was reconstructed. In (f), the peaks are more distinct and the gray level range is smaller. The effect of having brighter image edges, as it was the case in Figure 13(c), is even more pronounced in Figure 14(e). Changing the  $\delta/\beta$  ratio to 75 in the SD reconstruction (Figure 14(h)) leads to a distribution that looks more similar to Figure 14(d).

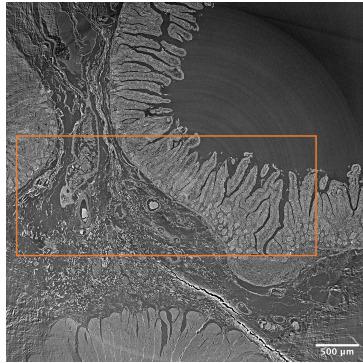




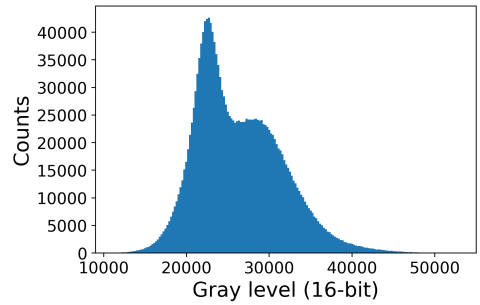
(a) Micro-CT with  $\delta/\beta = 217.6$



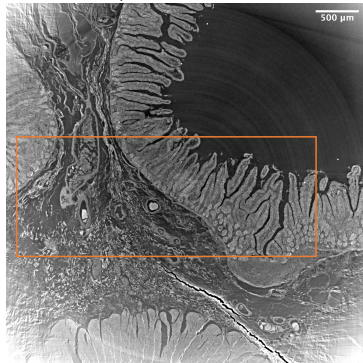
(b) Micro-CT with  $\delta/\beta = 217.6$



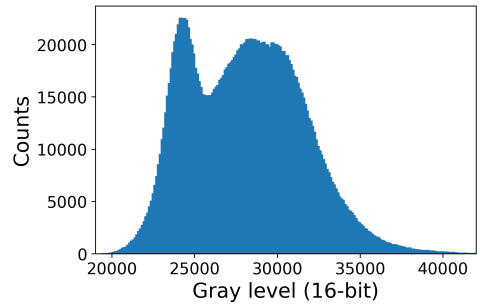
(c) TOMCAT (direct) with  $\delta/\beta = 217.6$



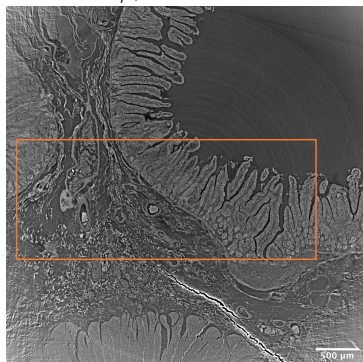
(d) TOMCAT (direct) with  $\delta/\beta = 217.6$



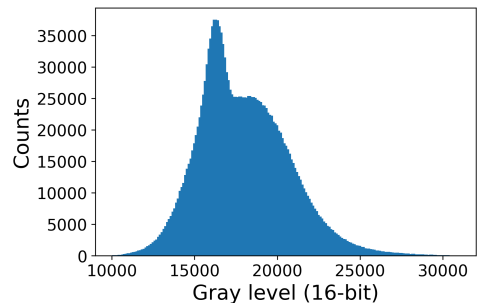
(e) TOMCAT (SD) with  $\delta/\beta = 217.6$



(f) TOMCAT (SD) with  $\delta/\beta = 217.6$



(g) TOMCAT (SD) with  $\delta/\beta = 75$



(h) TOMCAT (SD) with  $\delta/\beta = 75$

**Figure 14:** Reconstructed images ( $4 \times$  magnification) and corresponding histograms with phase retrieval. The TOMCAT data was additionally reconstructed using SD Python scripts. The orange boxes show the regions that were used to create the histograms.

## 4.2 Comparison of Setups

This section deals with the comparison of the two setups, as well as the comparison of the direct vs. SD reconstruction in case of the TOMCAT data, in terms of CNR and resolution. In order to make statements about contrast, a 3D segmentation of the same blood vessel was performed with the procedure described in Section 3.4. Each one 2D slice of the segmented blood vessel for the micro-CT and two TOMCAT (direct and SD) datasets is shown in Figure 15. Here, it is distinguished between the reconstruction without phase retrieval ((a)-(c)) and with phase retrieval ((d)-(f)).

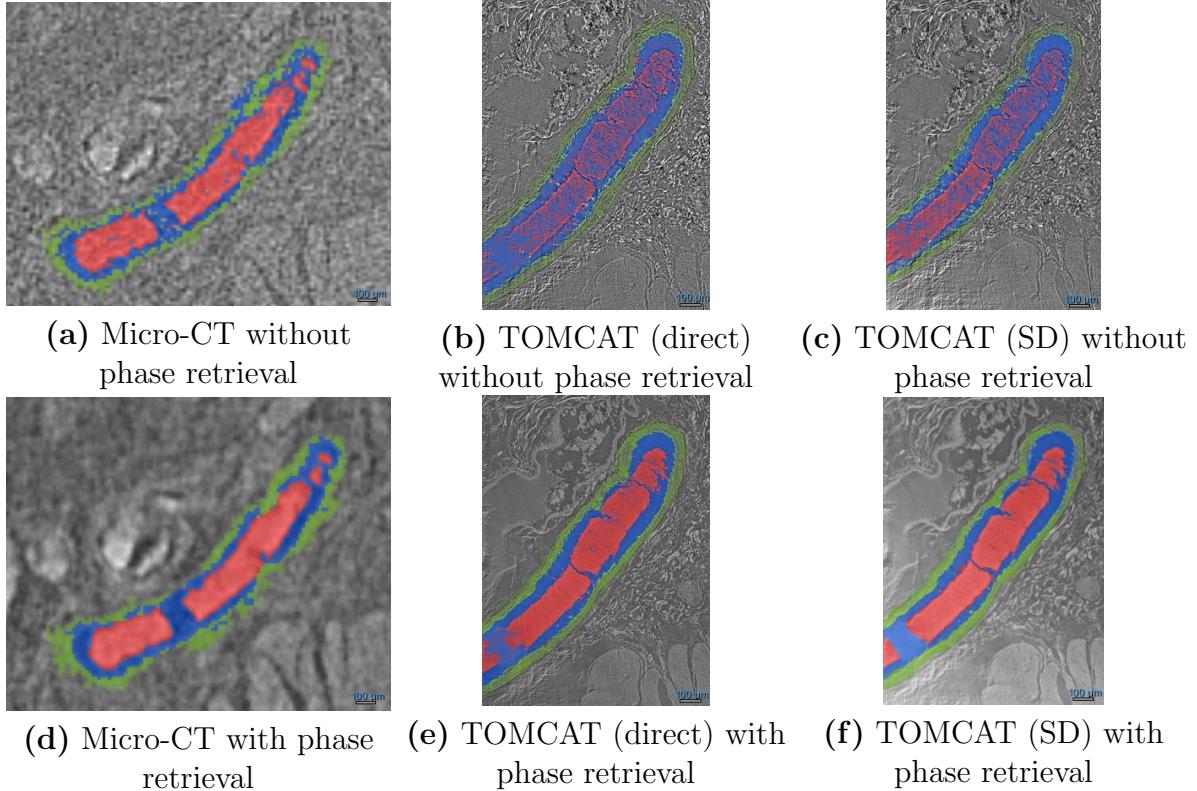


**Figure 15:** Segmented blood vessels with the segments being blood (red), vessel wall (green) and paraffin background (blue). For the phase retrieval, a  $\delta/\beta$  ratio of 217.6 was used.

In Figure 15 it can be seen that the blood vessel was partitioned into three segments: blood (red), vessel wall (green) and background (blue), with the background being paraffin. The complete 3D blood vessel resulting from the direct reconstruction of the phase retrieved TOMCAT data is illustrated in Figure 16.

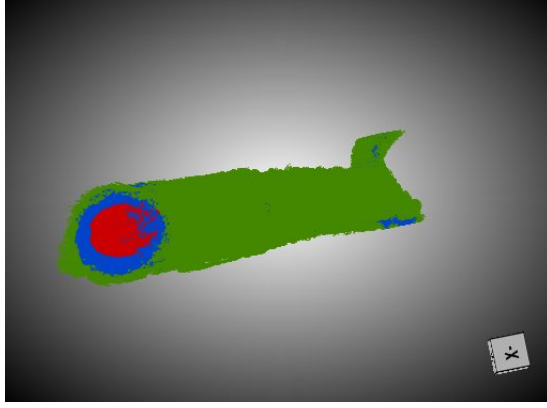


**Figure 16:** 3D blood vessel from direct TOMCAT reconstruction with  $\delta/\beta = 217.6$ .

To perform a meaningful comparison between the setups and used reconstruction methods, their individual CNRs were analyzed. In order to calculate the CNRs, the mean intensities and corresponding standard deviations of the different segments were extracted using the *Dragonfly* software. As the contrast between two segments is just their intensity difference, it can be directly calculated from the intensity values. This means that the contrast  $C$  depends on the intensity values  $I_A$  and  $I_B$  of the segments  $A$  and  $B$ :  $C = |I_A - I_B|$ .

The standard deviation of the intensity values of the individual segments can be interpreted as their noise. To obtain the noise of the contrast between two segments  $A$  and  $B$ , it is assumed that the individual standard deviations are not correlated, i.e. the total noise  $\sigma_0$  is defined as  $\sigma_0 = \sqrt{\sigma_A^2 + \sigma_B^2}$  [38].

The extracted mean intensity values and their standard deviations as well as the calculated contrasts and CNR values are shown in Table 3 and Table 4 for the images reconstructed without and with phase retrieval, respectively. For the reconstructions with phase retrieval a  $\delta/\beta$  ratio of 217.6 was used. For a better evaluation of the SD approach, reconstructions resulting from different  $\delta/\beta$  ratios would be desirable, but image segmentation is a time-consuming process that could only be performed to a limited extent within the framework of this thesis. To compare the reconstructions resulting from the same initial conditions, the same  $\delta/\beta$  ratio was used in all three cases.

**Table 3:** Mean intensities, corresponding standard deviations  $\sigma$  and calculated contrasts and CNRs for the segments blood (b), vessel wall (w) and background (bg) (no phase retrieval).

	Micro-CT	TOMCAT (direct)	TOMCAT (SD)
Intensity of b with $\sigma$	$1.3 \cdot 10^4 \pm 1.8 \cdot 10^3$	$3.8 \cdot 10^4 \pm 6.5 \cdot 10^3$	$3.8 \cdot 10^4 \pm 6.0 \cdot 10^3$
Intensity of w with $\sigma$	$1.1 \cdot 10^4 \pm 1.2 \cdot 10^3$	$3.9 \cdot 10^4 \pm 6.3 \cdot 10^3$	$3.9 \cdot 10^4 \pm 6.7 \cdot 10^3$
Intensity of bg with $\sigma$	$0.78 \cdot 10^4 \pm 1.5 \cdot 10^3$	$2.5 \cdot 10^4 \pm 6.1 \cdot 10^3$	$2.4 \cdot 10^4 \pm 5.6 \cdot 10^3$
Contrast ( $ b-w $ )	$2.0 \cdot 10^3$	$1.0 \cdot 10^3$	$1.0 \cdot 10^3$
Contrast ( $ b-bg $ )	$5.2 \cdot 10^3$	$1.3 \cdot 10^4$	$1.4 \cdot 10^4$
Contrast ( $ w-bg $ )	$3.2 \cdot 10^3$	$1.4 \cdot 10^4$	$1.5 \cdot 10^4$
CNR ( $ b-w $ )	0.9245	0.1105	0.1112
CNR ( $ b-bg $ )	2.2193	1.4584	1.7058
CNR ( $ w-bg $ )	1.6659	1.5965	1.7178

**Table 4:** Mean intensities, corresponding standard deviations  $\sigma$  and calculated contrasts and CNRs for the segments blood (b), vessel wall (w) and background (bg) (with phase retrieval,  $\delta/\beta = 217.6$ ).

	Micro-CT	TOMCAT (direct)	TOMCAT (SD)
Intensity of b with $\sigma$	$5.5 \cdot 10^4 \pm 2.6 \cdot 10^3$	$3.5 \cdot 10^4 \pm 3.6 \cdot 10^3$	$4.3 \cdot 10^4 \pm 4.3 \cdot 10^3$
Intensity of w with $\sigma$	$5.1 \cdot 10^4 \pm 1.0 \cdot 10^3$	$3.2 \cdot 10^4 \pm 3.3 \cdot 10^3$	$4.0 \cdot 10^4 \pm 4.1 \cdot 10^3$
Intensity of bg with $\sigma$	$4.7 \cdot 10^4 \pm 1.8 \cdot 10^3$	$2.3 \cdot 10^4 \pm 3.1 \cdot 10^3$	$3.4 \cdot 10^4 \pm 5.2 \cdot 10^3$
Contrast ( $ b-w $ )	$4.0 \cdot 10^3$	$3.0 \cdot 10^3$	$3.0 \cdot 10^3$
Contrast ( $ b-bg $ )	$8.0 \cdot 10^3$	$1.2 \cdot 10^4$	$9.0 \cdot 10^3$
Contrast ( $ w-bg $ )	$4.0 \cdot 10^3$	$9.0 \cdot 10^3$	$6.0 \cdot 10^3$
CNR ( $ b-w $ )	1.4359	0.6143	0.5049
CNR ( $ b-bg $ )	2.5298	2.5259	1.3338
CNR ( $ w-bg $ )	1.9426	1.9878	0.9061

Having a look at Table 3 leads to the observation that all CNRs are larger for the micro-CT setup compared to the TOMCAT setup. The blood-wall CNR is almost identical for the direct and SD reconstruction of the TOMCAT data, whereas the blood-background and wall-background CNRs are slightly higher in case of the SD TOMCAT data.

Table 4 reveals that the CNR values are larger than their corresponding equivalents in Table 3 for the micro-CT and direct TOMCAT data. In case of the SD TOMCAT data this is only true for the blood-wall CNR. The blood-background and wall-background CNRs of the phase-retrieved SD TOMCAT data are smaller than their corresponding values in Table 3. The blood-wall CNR is significantly larger for the micro-CT data, whereas its blood-background CNR is only slightly higher and its wall-background CNR even slightly smaller when comparing to the direct TOMCAT data. The CNRs resulting from the direct TOMCAT reconstruction are higher than the ones obtained from the SD reconstruction of the TOMCAT data in all cases.

The two setups were compared with regards to resolution with the aim to find out if the identification of the ganglia (and hence neurons) is possible. When the ganglia could be resolved, some exemplary ganglia were marked by arrows. This is illustrated for the two setups in Figure 17 (a) and (b) for reconstructions without phase retrieval and (c) and (d) for reconstructions with phase retrieval. It can be seen that an identification of the ganglia in case of the absorption contrast image recorded with the micro-CT setup (Figure 17 (a)) is not possible. Their identification in Figure 17 (b)-(d) is successful, with the ganglia's best visibility delivered by the phase retrieved TOMCAT data (Figure 17 (d)).

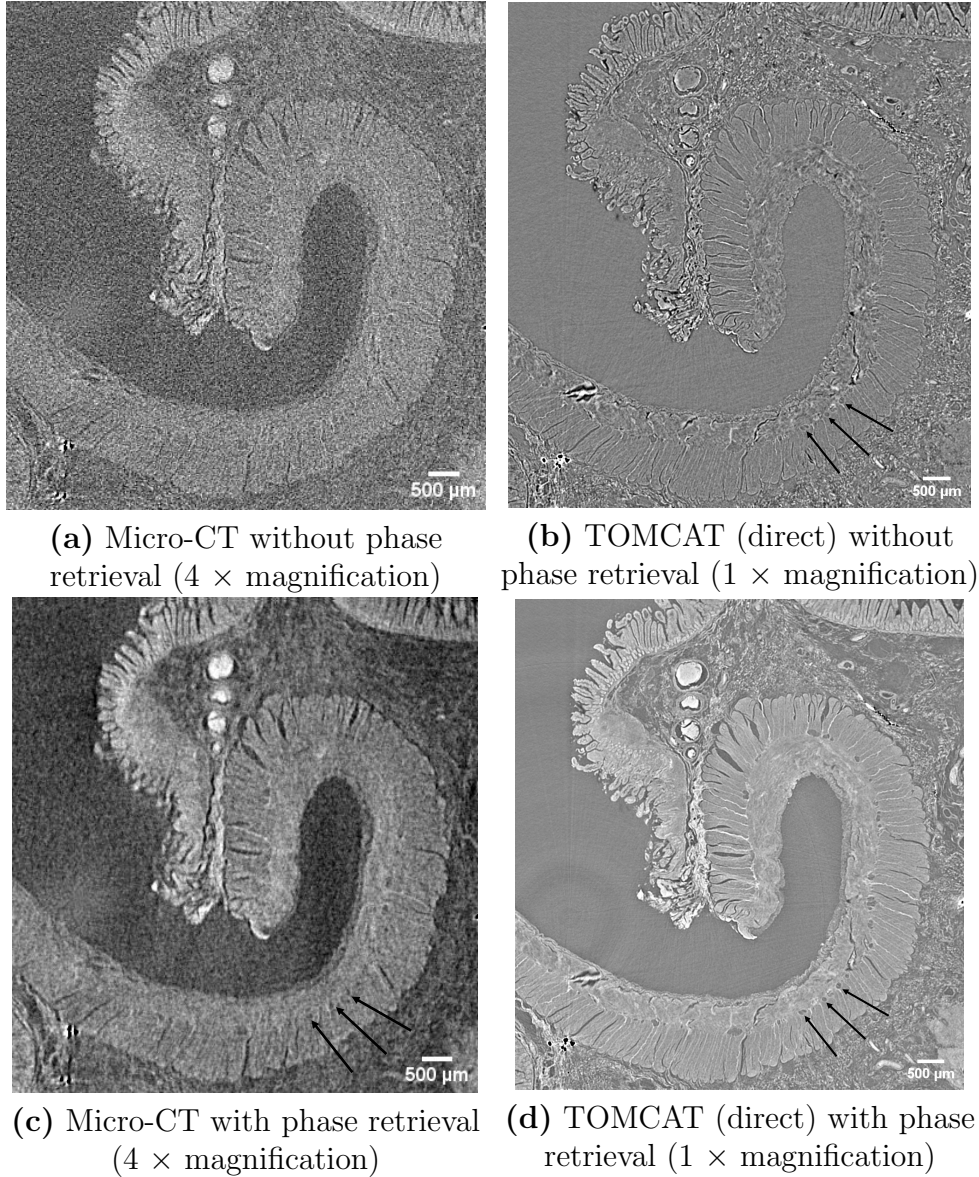


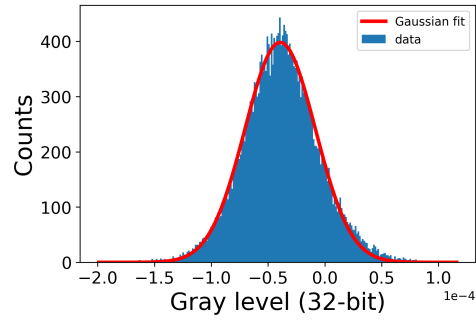
**Figure 17:** Reconstructed images of the overall sample. The arrows indicate the presence of ganglia.

### 4.3 Optimization of Phase Contrast for Micro-CT

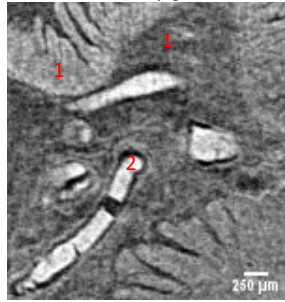
In order to get the best phase contrast, several parameters can be tuned and their influence on the image quality will be described in Section 5.4. Here, the aim was to find the best  $\delta/\beta$  ratio for the lab based setup with the purpose of contrast enhancement. This section presents several reconstructions of the images recorded by the micro-CT with  $\delta/\beta = 21.76, 217.6, 1000$  and  $2176$ . The images and corresponding histograms are shown in Figure 18. For the histograms, the peaks were fitted using Gaussian distributions. In order to give an orientation about which parts of the image contribute to which part of the histogram, numbers were used to assign the image parts to the peaks. Figure 18(b) has only one peak with all parts of (a) contributing to it. In case of Figure 18(d), it can be distinguished between high-intensity biological features (2) and background/low-intensity biological features (1) (see Figure 18(c)). For Figure 18(f) and (h) there are four peaks: the background (1) and three different kinds of biological tissue (2-4).



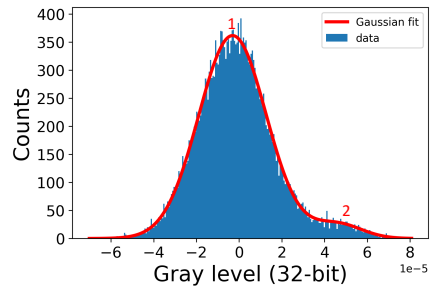
(a) Reconstruction with  $\delta/\beta = 21.76$



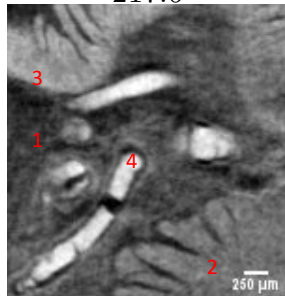
(b) Histogram with  $\delta/\beta = 21.76$



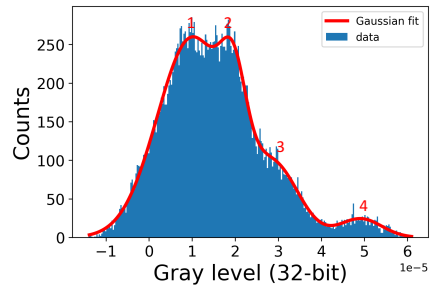
(c) Reconstruction with  $\delta/\beta = 217.6$



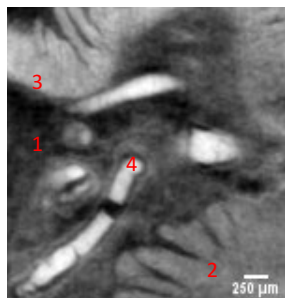
(d) Histogram with  $\delta/\beta = 217.6$



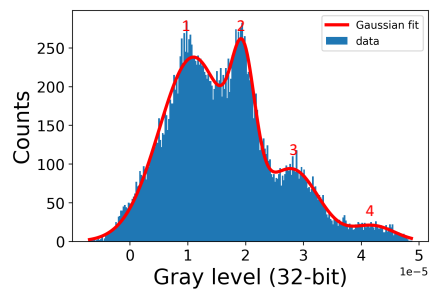
(e) Reconstruction with  $\delta/\beta = 1000$



(f) Histogram with  $\delta/\beta = 1000$



(g) Reconstruction with  $\delta/\beta = 2176$



(h) Histogram with  $\delta/\beta = 2176$

**Figure 18:** Reconstructed images ( $4 \times$  magnification) and corresponding histograms obtained by the micro-CT setup with different  $\delta/\beta$  ratios. The peaks of the histograms were fitted by Gaussian distributions. The numbers give an orientation about which parts of the images contribute to which peak in the histogram.

There are several aspects that can be observed in Figure 18. First, the image quality, i.e. the resolution, decreases with increasing  $\delta/\beta$  ratio. Second, the histograms show distributions with more and better distinguishable peaks with increasing  $\delta/\beta$  ratios. More peaks correspond to being able to better distinguish between different parts of the image. In order to find the optimal  $\delta/\beta$  ratio for contrast improvement, it would be best to determine and compare the different CNRs. However, as was pointed out in Section 4.2, the image segmentation needed for this procedure is time-consuming and was not feasible in the scope of this thesis. In addition, as will be discussed in Section 5.1, the extracted CNRs seem to be unreliable. As an alternative approach to get an impression about what  $\delta/\beta$  ratio is best, the SNRs of the different images was analyzed instead. The noise is assumed to be given by the full width at half maximum (FWHM) of the background peak, only clearly visible in Figure 18(f) and (h), which is why a SNR analysis only makes sense for these two cases. The signals of the different biological tissues are assumed to be the difference between the expectation value  $\mu$  of the corresponding peak to the expectation value of the background peak. The Gaussian fits were used to find these values and are listed in Table 5.

**Table 5:** SNR for different  $\delta/\beta$  ratios for the micro-CT data.

	$\delta/\beta = 1000$	$\delta/\beta = 2176$
Noise (FWHM 1)	$1.9153 \cdot 10^{-5}$	$1.4004 \cdot 10^{-5}$
Signal 2 ( $\mu_2 - \mu_1$ )	$0.9587 \cdot 10^{-5}$	$0.8628 \cdot 10^{-5}$
Signal 3 ( $\mu_3 - \mu_1$ )	$1.9413 \cdot 10^{-5}$	$1.7246 \cdot 10^{-5}$
Signal 4 ( $\mu_4 - \mu_1$ )	$3.9037 \cdot 10^{-5}$	$3.1039 \cdot 10^{-5}$
SNR 2	0.5005	0.6161
SNR 3	1.0136	1.2315
SNR 4	2.0382	2.2164

Overall it can be seen that it is impossible to distinguish between the different parts of the image in Figure 18(b). In Figure 18(d) the high-intensity biological tissue can be identified, but the background cannot be extracted. From Table 5 it becomes apparent that the SNR increases with increasing  $\delta/\beta$  ratio.

#### 4.4 Segmentation of Ganglia

As could be seen in Figure 17(d), the ganglia could be best identified within the images reconstructed from the TOMCAT data with phase retrieval. Since the ganglias' visibility is crucial for their successful segmentation, the high-resolution TOMCAT dataset was used for this purpose. The ganglia (red) were segmented within a  $0.5 \text{ mm}^3$  volume and separated from the background (blue) and remaining biological tissue (green), as can be seen in Figure 19. The volumes of the ganglia, remaining biological tissue and background were determined to be  $0.011 \text{ mm}^3$ ,  $0.44 \text{ mm}^3$  and  $0.067 \text{ mm}^3$ .

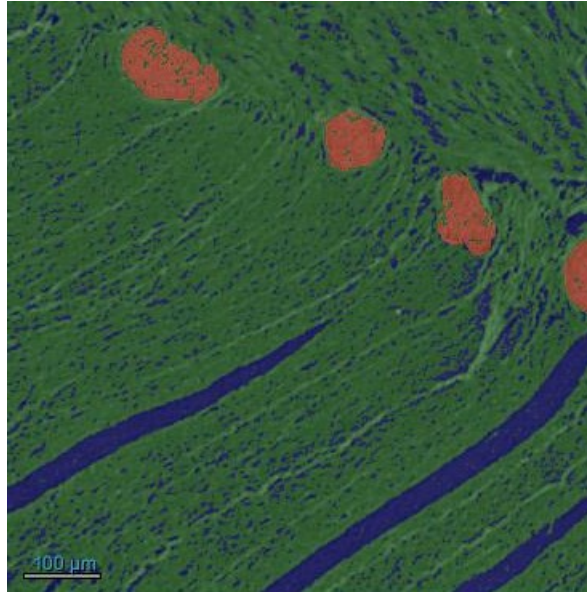


**Figure 19:** Segmentation of the ganglia (red) in a  $0.5 \text{ mm}^3$  volume of the sample. The background is blue and the remaining biological tissue is green.



## 5 Discussion

The actual interpretation of the results is presented in this section. The research questions formulated in Section 1 are addressed and answered: What requirements need to be fulfilled to image ganglia and successfully segment them subsequently? Is phase contrast needed for this purpose and how can it be improved? Overall, the whole procedure for segmenting the ganglia is evaluated and optimized.

First, the two setups are compared and the differences and their influence on the images is discussed in Section 5.1. This is followed by taking up the need of phase contrast images (Section 5.2) and the evaluation of the SD reconstruction of the TOMCAT data (Section 5.3). Afterwards, it is argued which is the best  $\delta/\beta$  ratio for the micro-CT setup in Section 5.4, followed by debating the impact of ganglia segmentation on understanding the enteric nervous system (ENS) in Section 5.5.

### 5.1 Comparison of Setups

The purpose of comparing the two setups is to find out what requirements have to be fulfilled in order to visualize and successfully segment the ganglia. Therefore, the results from Section 4.2 are explained with the background of the different setup properties. As could be seen, the CNRs obtained from image segmentation were different for the two setups, i.e. the CNRs resulting from the micro-CT setup were significantly higher than the ones from the TOMCAT setup (see Table 3). This is surprising because the expectation would be the reverse. Since synchrotron radiation delivers a significantly larger photon flux, the contrast should be larger for the TOMCAT setup. This indicates a problem in the evaluation of the CNR and raises the question whether the obtained values can be trusted.

To address this question, the histograms of the background segment based on the absorption contrast images for both setups are shown in Figure 20. In case of the micro-CT (Figure 20(a)), no clear peak can be identified, suggesting that signal from the biological tissue also contributes to this distribution. In contrast, the TOMCAT histogram (Figure 20(b)) shows a clearly identifiable peak that can be assigned to the background. Consequently, the histogram in Figure 20(a) seems to be unreliable, which means that the extracted mean and standard deviation are biased. This leads to the conclusion that the CNRs from the TOMCAT setup seem to be more reliable, which does not mean that they can be assumed to be correct. Overall, the method used here is not suitable to determine and compare CNRs.

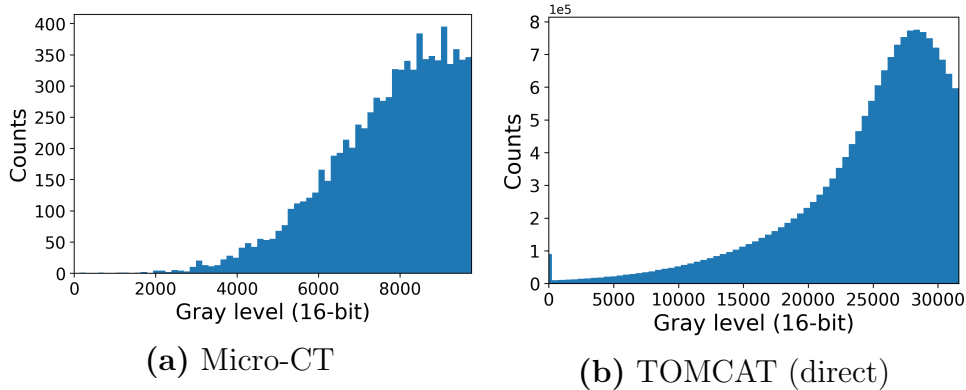


**Figure 20:** Histograms of absorption contrast based images corresponding to the segmented background.

The same problem occurred in case of the phase contrast images, as can be seen in Figure 21 in the Appendix. Consequently, the CNRs in Table 4 cannot be used for comparing the two setups, too. However, one trend that was observed when comparing the CNRs of the same setups in Table 3 and 4, is as expected: the CNRs were in general larger than their corresponding CNR values from Table 3. On the one hand, considering phase contrast leads to edge enhancement, subsequently improving contrast, as was described in Section 2.1.2. On the other hand, the *Paganin* algorithm acts as low-pass filter, thus reducing high-frequency noise (Section 3.3.1). This leads to the overall increase of the CNR.

From this it cannot be concluded which setup is superior as the determined CNRs are assumed to be incorrect. However, the effect of the *Paganin* algorithm on decreasing the noise could be illustrated vividly. In general, it was shown in Figure 15 that a segmentation was possible in all cases, but the corresponding histograms raise the question of how successful the determination of the individual CNRs was, especially in case of the micro-CT. What made the segmentation itself a challenging process was not the contrast, but particularly the resolution, which is discussed in the following.

As was illustrated in Figure 17, the ganglias' visibility was best in case of the phase retrieved TOMCAT data. Here, it has to be distinguished between two factors: resolution and contrast mechanism. The effect of the phase contrast on the ganglias' visibility is discussed in Section 5.2. The resolution of the TOMCAT setup is higher because of the smaller effective pixel size. As listed in Table 1 and 2, the micro-CT had an effective pixel size of  $18.75\ \mu\text{m}$ , whereas TOMCAT delivered effective pixel sizes of  $6.5\ \mu\text{m}$  ( $1 \times$  magnification) and  $1.625\ \mu\text{m}$  ( $4 \times$  magnification).

One can wonder now if it is possible to decrease the effective pixel size of the micro-CT to a value comparable to the effective pixel size of TOMCAT. The answer is yes, increasing the magnification by adapting the source-sample and source-detector distances (geometric magnification) will decrease the effective pixel size. However, a resolution as low as the one delivered by TOMCAT will not be achieved. This is due to the different detection systems. The direct detection system of the micro-CT setup (single photon counting) is based on geometric magnification, whose resolution is additionally limited by the source spot size ( $20\ \mu\text{m} \times 80\ \mu\text{m}$ ). This means that reducing the effective pixel size into the single-digit micrometer range will cause blurring of the image. This is not true for the TOMCAT setup, as it has an indirect detection system (X-rays are converted to visible light via a scintillator), that uses an optical microscope for magnification, leading

to the resolution not being dependent on the source spot size [39, 40].

A requirement that needs to be met for phase contrast imaging is spatial coherence. This is achieved by having source spot sizes as small as possible, which will lead to a decrease in photon flux and hence signal. As synchrotrons deliver radiation of higher brightness (and photon flux), the exposure time and radiation dose can be drastically decreased when performing experiments at such facilities. This leads to the practical aspect of time consumption, which makes the TOMCAT setup superior to the micro-CT setup [41].

This leads to the conclusion that synchrotron radiation is not necessarily a requirement to perform phase contrast imaging, but is advantageous in terms of time and radiation dose. However, the most important aspect is the resolution that differs due to the differences in detection systems. This is the main reason that makes the TOMCAT setup superior to the micro-CT setup because a higher resolution leads to a less ambiguous image segmentation.

Even though the micro-CT setup delivers lower resolutions, it can be a useful tool for overview scans of the sample. As could be seen in Figure 17(c), it is sufficient to identify the ganglia and hence a ROI that can be scanned with a higher resolution setup.

## 5.2 Comparison of Contrasts

As the requirements for phase contrast imaging are much more complicated to fulfill than the ones for conventional absorption based imaging because a spatially coherent beam is needed, the question arises if phase contrast is necessary for the segmentation of the ganglia. In Section 2.1.2 it was described that the advantage of phase contrast is given by edge enhancement. In addition, absorption contrast is weak for biological tissue because it has similar absorption properties and does not absorb much radiation in general. Consequently, phase contrast imaging leads to a non-negligible improvement in contrast. This could not only be seen subjectively on the reconstructed images in Figure 13 and 14, but also in the corresponding histograms. The histograms of the images reconstructed without phase retrieval consist of only one peak, with all parts of the sample contributing to it. That makes a separation of the different parts of the sample less obvious. The histograms resulting from applying phase retrieval show two peaks, making a separation between background and biological tissue more explicit. Although segmentation is generally possible in all cases, it reduces mistakes in the assignment of image pixels to certain sample components when the contrast is increased, since this leads to a more obvious separation between different parts of the sample.

## 5.3 Evaluation of Self-Developed Reconstruction

This section continues the discussion of the two different contrasts, shifting the focus to whether the SD reconstruction of the TOMCAT data was successful. When looking at the reconstructed images in Figure 13(b) and (c), it can be seen that the images look almost identical, indicating a successful reconstruction using the SD approach. However, what can be seen in Figure 13(c) is that the edges of the image are slightly brighter compared to Figure 13(b). That can be explained by an imperfect padding procedure in case of the SD reconstruction. Here, the padding was performed with the edge values of the array. The padding procedure of the direct TOMCAT reconstruction is not known.

The histograms in Figure 13(e) and (f) support the statement of a successful recon-

struction, as they show a similar gray level range and distribution shape. From Table 3 it could be seen that the CNRs for the direct and SD reconstruction were similar, with the SD reconstruction having slightly higher values. It is not unlikely that a subjective segmentation might play a role in these deviations. The bright image edges described above might have an impact, too. In addition, as was discussed in Section 5.1, it cannot be assumed that the CNRs are correct. As this section discusses the same setup, namely the TOMCAT setup, a comparison in terms of the CNR was still conducted.

In case of the reconstruction using phase retrieval with  $\delta/\beta = 217.6$ , more differences become apparent. The blood-background and wall-background CNRs listed in Table 4 are significantly higher for the direct TOMCAT reconstruction, whereas the blood-wall CNR is only slightly larger. This can be explained when looking at the histograms in Figure 14(d) and (f). The intensity values of the background and biological tissue from Table 4 do match with the first and second histogram peak in Figure 14(d), respectively, for the direct reconstruction. This is not true for the SD reconstruction. The background and biological tissue intensities can only be assigned to the second peak in Figure 14(f). The reason for this is given by the gradient in intensity that is pronounced on the image edges in Figure 14(e). As the *Paganin* algorithm enhances edges and hence intensity differences, the brighter image edges are more emphasized in the phase contrast image compared to the absorption contrast image that was discussed before and the not sufficient padding becomes apparent even more. Therefore, the first peak in Figure 14(f) corresponds to the background as well, but brighter parts of the background are part of the second peak, i.e. the separation between background and biological tissue was not successful. That is why the contrasts (and thus CNRs) between the biological tissue and background are smaller for the SD reconstruction compared to the direct one. Nevertheless, an image segmentation is still possible, even though it is less obvious when using thresholding with the *Otsu* method.

The image reconstruction and corresponding histograms can be manipulated by varying some parameters of Equation (24). This will be discussed in detail in Section 5.4. By setting  $\delta/\beta$  to 75, as it was done for Figure 14(g) and (h), the edge enhancement is decreased and hence the histogram distribution becomes more similar to the one from the direct reconstruction.

In summary, it can be concluded that the SD reconstruction did work, but was not as optimal as the direct one. Since the detailed procedure of the direct reconstruction is unknown, a further comparison is impossible. The fact that the direct reconstruction delivered better results is most likely due to the fact that it was optimized for user operation. In order to improve the SD approach, one could think about looking into other padding procedures or simply masking the image.

## 5.4 Optimization of Phase Contrast for Micro-CT

An optimization for the micro-CT phase retrieval procedure was not performed yet and is part of this section. From Equation (24), the following can be seen:

1. By tuning some parameters, the phase and hence the reconstructed image can be influenced. These parameters, are the energy (proportionally related to the wave vector  $\mathbf{k}_\perp$ ), propagation distance  $z$  and  $\delta/\beta$  ratio. Here, it was tried to find the optimal value for the latter, as this parameter is not set by the experimental setup.

2. As was discussed in Section 3.3.1, the *Paganin* algorithm acts as a low-pass filter and the higher the  $\delta/\beta$  ratio, the more high-frequency noise is filtered out. However, this decreases the image resolution as a consequence.

The SNRs in Table 5, resulting from the histograms in Figure 18, showed an increase in SNR with increasing  $\delta/\beta$  ratio. As was mentioned in Section 4.3, the noise could not be extracted in case of Figure 18(b) and (d) and could only be obtained from the histograms in Figure 18(f) and (h). Overall, it was shown that the SNR increases with increasing  $\delta/\beta$  ratio. That is because an increase in  $\delta/\beta$  leads to noise reduction. In principle, that would mean that the higher  $\delta/\beta$  ratio, the better the reconstructed image. As can be seen in the images that correspond to the histograms, this is not the case. When looking at the images subjectively, one sees that the image quality of the highest  $\delta/\beta$  ratio (2176) is not the best. That is because by filtering out high-frequency values, the image resolution is decreased. Therefore, in order to determine the best  $\delta/\beta$  ratio, one has to trade-off between resolution and SNR. The resolution should still be as high as possible in order to make image segmentation feasible. The images in Figure 18(e) and (g) appear to be too blurry for this purpose, which is why the standard  $\delta/\beta$  ratio of 217.6 is confirmed to be the most optimal one for the micro-CT setup due to this trade-off.

## 5.5 Segmentation of Ganglia

After optimizing and justifying the procedure used to obtain the images for the segmentation of the ganglia, the results of the segmented ganglia are addressed. Even though the volume could be successfully determined, it is meaningless as of now. That is because only a small volume of one sample was investigated in the scope of this thesis, as the image segmentation procedure is a time-consuming process. In order to compare the extracted volume of the ganglia to that of other patients and get statistically significant results, the ganglias' volume in a larger sample volume (here  $0.5 \text{ mm}^3$ ) and of more patients should be determined. Nevertheless, a workflow for the successful ganglia segmentation was developed and the analysis of this one sample lays the cornerstone for studying chronic bowel diseases caused by changes in the ENS in detail.

## 6 Conclusion

Enteric neuropathy is an intestinal disease that causes changes of the ENS. If the neurons, that make up the ganglia, in the ENS are abnormal, this can lead to a broad spectrum of symptoms, including nausea, pain, diarrhea and vomiting. It happens that patients suffering from enteric neuropathy get a wrong diagnosis, but a correct diagnosis and understanding of the disease are important for successful treatment. In the scope of this thesis, different experimental setups and approaches for the sufficient segmentation of the ganglia were compared and evaluated with the aim to improve the segmentation procedure.

In order to record 3D images of the ENS in intestinal samples, two different setups were used: A micro-CT in Lund (Sweden) and the TOMCAT beamline of SLS in Villigen (Switzerland). X-ray tomography was used for this purpose and the obtained images were either based on absorption or phase contrast. For the latter, the *Paganin* algorithm was used for the phase retrieval, as the phase cannot be detected directly.

These two setups were compared in terms of CNR and resolution in Section 5.1. It was found that the determined CNRs should not be trusted, especially in case of the micro-CT, because a clear separation between the different segments was not visible in the corresponding histograms. From this, it was concluded that the method used here for evaluating the CNRs of the different setups is not suitable. The resolution was better for the TOMCAT setup due to using an optical microscope for magnification, which makes the effective pixel size independent from the source spot size. Furthermore, it was discussed that using synchrotron radiation is no requirement for this specific experiment, but can be advantageous as its high brightness leads to lowering exposure time and thus radiation dose. What is required, however, is a resolution as high as possible for the successful segmentation of ganglia, which could not be delivered by the micro-CT setup.

As biological tissue has similar absorption properties, the image contrast can be drastically improved when using phase retrieval, as was discussed in Section 5.2. During this process, edge enhancement takes place and different features can be distinguished better from each other.

In Section 5.3, the self-developed reconstruction of the TOMCAT data was found to be working in general, but the results were not optimal, especially in case of the reconstruction with phase retrieval. The separation between background and biological tissue was not successful in comparison to the reconstruction that was directly performed at the beamline. The reason for this was a not optimal padding of the image, leading to the creation of an intensity gradient within the image. A segmentation was still possible, but more biased due to this reason. By varying the  $\delta/\beta$  ratio, the result obtained by the self-developed reconstruction became more similar to the reconstruction directly performed at the beamline. A further comparison was impossible, as the details of the beamline's reconstruction procedure are unknown.

The influence of varying  $\delta/\beta$  values (21.76, 217.6, 1000 and 2176) on the image reconstruction with phase retrieval was investigated and optimized for the micro-CT in Section 5.4. It was found that a higher  $\delta/\beta$  ratio leads to an increase in SNR, but decrease in resolution. It was concluded that in principle the highest SNR, and hence highest  $\delta/\beta$  ratio of 2176 would be best, but the image resolutions when using the  $\delta/\beta$  ratios 1000 and 2176 were not high enough for a sufficient segmentation of the ganglia. Consequently, it has to be compromised between SNR and resolution and the  $\delta/\beta$  value of 217.6 was confirmed to be the most appropriate one among 21.76, 217.6, 1000 and 2176.

Using the phase retrieved TOMCAT dataset, the ganglia in a  $0.5 \text{ mm}^3$  were segmented for one sample and their volume was determined to be  $0.011 \text{ mm}^3$ . The segmentation was performed by applying thresholding based on the *Otsu* method. The volumes of the remaining biological tissue and background were  $0.44 \text{ mm}^3$  and  $0.067 \text{ mm}^3$ , respectively. In Section 5.5 it was discussed that the obtained volumes make no human impact, as no data for comparison is available yet.

In conclusion, the successful workflow for the studies of ganglia in the ENS was found to consist of the recording of 3D images with a resolution in the order of  $4.875 \mu\text{m}$  and the reconstruction using phase retrieval. The ganglia could be successfully separated from the other biological components of the sample, however, further studies on the ENS are necessary to obtain statistically relevant results.

## 7 Outlook

This thesis lays the foundation for improving the segmentation of ganglia from 3D images of intestinal samples, paving the way for a better understanding of enteric neuropathy caused by changes of the ENS and thus an impact on human health. The pipeline for data acquisition as well as image reconstruction and image segmentation has been successfully carried out for a  $0.5 \text{ mm}^3$  volume of an intestinal sample.

In future, as many ganglia volumes as possible should be determined in order to compare them to each other and obtain statistically significant results. To do this, the pipeline used in this thesis can be used to analyze the remaining data of the TOMCAT beamtime. In addition, data of more samples could be collected to increase the statistic significance.

The lab based micro-CT can be used in future to acquire overview scans of the sample, hence helping with identifying ROIs within them. An improvement of the lab based setup would also be conceivable. For example, data could be acquired with a nano-CT to evaluate if the resolution is comparable to that of the TOMCAT setup and therefore a realistic alternative to participating in beamtimes.



## References

- [1] A. D. Sperber, S. I. Bangdiwala, D. A. Drossman, U. C. Ghoshal, M. Simren, J. Tack, W. E. Whitehead, D. L. Dumitrescu, X. Fang, S. Fukudo, *et al.*, “Worldwide prevalence and burden of functional gastrointestinal disorders, results of rome foundation global study,” *Gastroenterology*, vol. 160, no. 1, pp. 99–114, 2021.
- [2] B. Ohlsson, R. Gustafsson, F. Swahn, E. Toth, B. Veress, and H. Thorlacius, “Endoscopic full-thickness biopsy, a novel method in the work up of complicated abdominal symptoms,” *Therapeutic advances in gastroenterology*, vol. 11, p. 1756283X17730747, 2018.
- [3] N. Peruzzi, B. Veress, L. B. Dahlin, T. Salditt, M. Andersson, M. Eckermann, J. Frohn, A.-L. Robisch, M. Bech, and B. Ohlsson, “3d analysis of the myenteric plexus of the human bowel by x-ray phase-contrast tomography—a future method?,” *Scandinavian journal of gastroenterology*, vol. 55, no. 10, pp. 1261–1267, 2020.
- [4] E. Boschetti, C. Malagelada, A. Accarino, J. R. Malagelada, R. F. Cogliandro, A. Gori, E. Bonora, F. Giancola, F. Bianco, V. Tugnoli, *et al.*, “Enteric neuron density correlates with clinical features of severe gut dysmotility,” *American Journal of Physiology-Gastrointestinal and Liver Physiology*, vol. 317, no. 6, pp. G793–G801, 2019.
- [5] D. McMorrow and J. Als-Nielsen, “Imaging,” in *Elements of modern X-ray physics*, ch. 9, pp. 305–340, John Wiley & Sons, 2 ed., 2011.
- [6] P. Willmott, “Imaging techniques,” in *An introduction to synchrotron radiation: techniques and applications*, ch. 8, pp. 367–402, John Wiley & Sons, 2 ed., 2019.
- [7] D. McMorrow and J. Als-Nielsen, “X-rays and their interaction with matter,” in *Elements of modern X-ray physics*, ch. 1, pp. 1–28, John Wiley & Sons, 2 ed., 2011.
- [8] C. Jacobsen, “X-ray physics,” in *X-ray Microscopy*, ch. 3, pp. 23–70, Cambridge University Press, 2020.
- [9] P. Willmott, “The interaction of x-rays with matter,” in *An introduction to synchrotron radiation: techniques and applications*, ch. 2, pp. 19–49, John Wiley & Sons, 2 ed., 2019.
- [10] D. McMorrow and J. Als-Nielsen, “Refraction and reflection from interfaces,” in *Elements of modern X-ray physics*, ch. 3, pp. 69–111, John Wiley & Sons, 2 ed., 2011.
- [11] C. Jacobsen, “Imaging physics,” in *X-ray Microscopy*, ch. 4, pp. 71–198, Cambridge University Press, 2020.
- [12] Y. Shechtman, Y. C. Eldar, O. Cohen, H. N. Chapman, J. Miao, and M. Segev, “Phase retrieval with application to optical imaging: a contemporary overview,” *IEEE signal processing magazine*, vol. 32, no. 3, pp. 87–109, 2015.
- [13] D. Paganin, S. C. Mayo, T. E. Gureyev, P. R. Miller, and S. W. Wilkins, “Simultaneous phase and amplitude extraction from a single defocused image of a homogeneous object,” *Journal of microscopy*, vol. 206, no. 1, pp. 33–40, 2002.

- [14] M. R. Howells, T. Beetz, H. N. Chapman, C. Cui, J. Holton, C. Jacobsen, J. Kirz, E. Lima, S. Marchesini, H. Miao, *et al.*, “An assessment of the resolution limitation due to radiation-damage in x-ray diffraction microscopy,” *Journal of electron spectroscopy and related phenomena*, vol. 170, no. 1-3, pp. 4–12, 2009.
- [15] Y. Kim, C. Kim, O. Y. Kwon, D. Nam, S. S. Kim, J. H. Park, S. Kim, M. Gallagher-Jones, Y. Kohmura, T. Ishikawa, *et al.*, “Visualization of a mammalian mitochondrion by coherent x-ray diffractive imaging,” *Scientific reports*, vol. 7, no. 1, pp. 1–9, 2017.
- [16] C. Jacobsen, “Radiation damage and cryo microscopy,” in *X-ray Microscopy*, ch. 1, pp. 457–495, Cambridge University Press, 2020.
- [17] P. Willmott, “Synchrotron physics,” in *An introduction to synchrotron radiation: techniques and applications*, ch. 3, pp. 51–106, John Wiley & Sons, 2 ed., 2019.
- [18] C. Jacobsen, “X-ray microscope instrumentation,” in *X-ray Microscopy*, ch. 7, pp. 259–320, Cambridge University Press, 2020.
- [19] Excillum, “X-ray tubes.” <https://www.excillum.com/history-of-x-rays-x-ray-tubes/>, Last accessed on 2022-11-10.
- [20] PSI, “The tomcat beamline.” <https://www.psi.ch/en/sls/tomcat/beamline-information>, Last accessed on 2022-12-11.
- [21] C. Jacobsen, “X-ray tomography,” in *X-ray Microscopy*, ch. 8, pp. 312–349, Cambridge University Press, 2020.
- [22] B. A. Dowd, G. H. Campbell, R. B. Marr, V. V. Nagarkar, S. V. Tipnis, L. Axe, and D. P. Siddons, “Developments in synchrotron x-ray computed microtomography at the national synchrotron light source,” in *Developments in X-ray Tomography II*, vol. 3772, pp. 224–236, SPIE, 1999.
- [23] D. Gürsoy, F. De Carlo, X. Xiao, and C. Jacobsen, “Tomopy: a framework for the analysis of synchrotron tomographic data,” *Journal of synchrotron radiation*, vol. 21, no. 5, pp. 1188–1193, 2014.
- [24] DECTRIS, “Technical specifications eiger2 r 500k.” [https://media.dectris.com/220921-Technical-specifications-DECTRIS\\_EIGER2\\_R\\_500K.pdf](https://media.dectris.com/220921-Technical-specifications-DECTRIS_EIGER2_R_500K.pdf), Last accessed on 2022-12-05.
- [25] R. Dinapoli, A. Bergamaschi, B. Henrich, R. Horisberger, I. Johnson, A. Mozzanica, E. Schmid, B. Schmitt, A. Schreiber, X. Shi, *et al.*, “Eiger: Next generation single photon counting detector for x-ray applications,” *Nuclear Instruments and Methods in Physics Research Section A: Accelerators, Spectrometers, Detectors and Associated Equipment*, vol. 650, no. 1, pp. 79–83, 2011.
- [26] K. Taguchi and J. S. Iwaczyk, “Vision 20/20: Single photon counting x-ray detectors in medical imaging,” *Medical physics*, vol. 40, no. 10, p. 100901, 2013.
- [27] T. Dreier, N. Peruzzi, U. Lundström, and M. Bech, “Improved resolution in x-ray tomography by super-resolution,” *Applied Optics*, vol. 60, no. 20, pp. 5783–5794, 2021.

- [28] CRYLINK, “Ce:luag crystal scintillator crystals.” [http://www.scintillator-crylink.com/wp-content/uploads/Ce\begin{group}\let\relax\relax\end{group}\[Pleaseinsert\Pre renderUnicode{}intopreamble\]LuAG-crystal-scintillator-crystals.pdf](http://www.scintillator-crylink.com/wp-content/uploads/Ce\begin{group}\let\relax\relax\end{group}[Pleaseinsert\Pre renderUnicode{}intopreamble]LuAG-crystal-scintillator-crystals.pdf), Last accessed on 2022-12-09.
- [29] G. Li, S. Luo, Y. Yan, and N. Gu, “A method of extending the depth of focus of the high-resolution x-ray imaging system employing optical lens and scintillator: a phantom study,” *Biomedical engineering online*, vol. 14, no. 1, pp. 1–14, 2015.
- [30] C. Jacobsen, “X-ray microscopes: a short introduction,” in *X-ray Microscopy*, ch. 1, pp. 1–3, Cambridge University Press, 2020.
- [31] M. Langer, Y. Zhang, D. Figueirinhas, J.-B. Forien, K. Mom, C. Mouton, R. Mokso, and P. Villanueva-Perez, “Pyphase—a python package for x-ray phase imaging,” *Journal of Synchrotron Radiation*, vol. 28, no. 4, pp. 1261–1266, 2021.
- [32] L. A. Feldkamp, L. C. Davis, and J. W. Kress, “Practical cone-beam algorithm,” *Josa a*, vol. 1, no. 6, pp. 612–619, 1984.
- [33] M. Lyra and A. Ploussi, “Filtering in spect image reconstruction,” *International Journal of Biomedical Imaging*, vol. 2011, 2011.
- [34] B. Münch, P. Trtik, F. Marone, and M. Stampanoni, “Stripe and ring artifact removal with combined wavelet—fourier filtering,” *Optics express*, vol. 17, no. 10, pp. 8567–8591, 2009.
- [35] Object Research Systems, “Dragonfly.” <https://www.theobjects.com/dragonfly/index.html>, Last accessed on 2022-11-14.
- [36] N. Otsu, “A threshold selection method from gray-level histograms,” *IEEE transactions on systems, man, and cybernetics*, vol. 9, no. 1, pp. 62–66, 1979.
- [37] D. Liu and J. Yu, “Otsu method and k-means,” in *2009 Ninth International Conference on Hybrid Intelligent Systems*, vol. 1, pp. 344–349, IEEE, 2009.
- [38] P. Ekström, *Statistics and the treatment of experimental data*. Lunds universitet, 1996.
- [39] H. Villarraga-Gómez, D. L. Begun, P. Bhattad, K. Mo, M. Norouzi Rad, R. T. White, and S. T. Kelly, “Assessing rechargeable batteries with 3d x-ray microscopy, computed tomography, and nanotomography,” *Nondestructive Testing and Evaluation*, pp. 1–17, 2022.
- [40] Zeiss, “Resolution of a 3d x-ray microscope.” <https://www.zeiss.com/content/dam/Microscopy/us/download/pdf/technical-notes/x-ray-microscopy/resolution-of-a-3d-x-ray-microscope.pdf>, Last accessed on 2022-12-01.
- [41] Excillum, “Phase-contrast imaging.” <https://www.excillum.com/x-ray-methods/x-ray-imaging/phase-contrast-imaging/>, Last accessed on 2022-12-01.

# Appendix

## Discussion of Reliability of the CNR

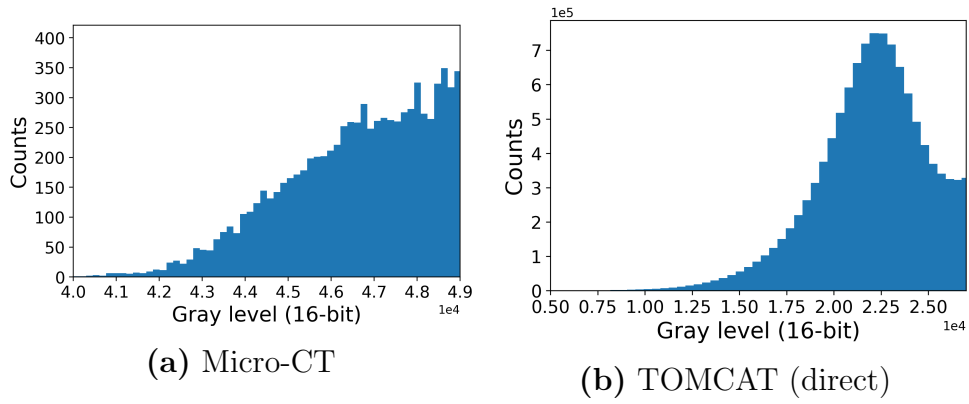


**Figure 21:** Histograms of phase contrast based images corresponding to the segmented background.

## Self-Developed Reconstruction without Phase Retrieval

```
1 import h5py
2 import numpy as np
3 import matplotlib.pyplot as plt
4 import tomopy
5 from PIL import Image, ImageOps
6
7 # Open file
8 with h5py.File('/data/staff/tomograms/users/julia/PSI_2022/061/
  ↪ 061_39_rescanned_x4_S04_.h5', 'r') as file:
9
10     # Find group
11     group_items = list(file.items())
12     group = file.get('exchange')
13
14     # Find dataset
15     dataset_items = list(group.items())
16
17     # Get data of selected slices
18     data = group.get('data')
19     proj = np.array(data[:, 599:900, :])
20     dark_data = group.get('data_dark')
21     dark = np.array(dark_data[:, 599:900, :])
22     flat_data = group.get('data_white')
23     flat = np.array(flat_data[:, 599:900, :])
24
25     # Flat-field correction
26     proj = tomopy.normalize(proj, flat, dark)
27
28     # Normalization
29     proj = np.divide(proj, np.max(proj))
30
31     # Logarithm
32     proj = tomopy.minus_log(proj)
33
34     # Create theta
35     theta = np.pi/180*np.linspace(0., 180., 1801, endpoint=False)
36
37     # Padding
38     proj = np.pad(proj, ((0,0), (0,0), (600, 600)), "edge")
39
40     # Reconstruction
41     recon = tomopy.recon(proj, theta, center=1282.13+600,
  ↪ algorithm='gridrec', sinogram_order=False, filter_name='parzen')
42
43     for i in range(301):
44         print("Next recon: ", i)
45         one_img = recon[i, :, :]
46
47
```

```

48     # float32 to uint16
49     one_img[np.where(one_img<-0.0007)] = -0.0007
50     one_img[np.where(one_img>0.0011)] = 0.0011
51     minimum = -0.0007
52     if minimum < 0:
53         one_img += abs(minimum)
54     maximum = 0.0011+np.abs(minimum)
55     one_img = one_img/maximum
56     one_img = one_img * 2**16-1
57     one_img = one_img.astype(np.uint16)
58
59     # Create image
60     PIL_image = Image.fromarray(one_img)
61
62     # Rotate image
63     PIL_image = PIL_image.rotate(270)
64
65     # Crop image
66     left = 600
67     top = 600
68     right = 3160
69     bottom = 3160
70
71     PIL_image_cropped = PIL_image.crop((left, top, right, bottom))
72
73     # Save image
74     PIL_image_cropped.save("/data/staff/tomograms/users/julia/Final
    ↪ Analysis/Absorption_Manual/tomo_{i}.tif".format(i))

```

## Self-Developed Reconstruction with Phase Retrieval

```
1 # Obtain phase information
2 import h5py
3 import numpy as np
4 import matplotlib.pyplot as plt
5 import pyphase
6 from pyphase import *
7 from PIL import Image, ImageOps
8
9 # Open file
10 with h5py.File('/data/staff/tomograms/users/julia/PSI_2022/061/
   ↪ 061_39_rescanned_x4_S04_.h5', 'r') as file:
11
12     # Find group
13     group_items = list(file.items())
14     group = file.get('exchange')
15
16     # Find dataset
17     dataset_items = list(group.items())
18
19     # Get data of selected slices
20     data = group.get('data')
21     proj = np.array(data[:, 625:815, :])
22     dark_data = group.get('data_dark')
23     dark = np.array(dark_data[:, 625:815, :])
24     flat_data = group.get('data_white')
25     flat = np.array(flat_data[:, 625:815, :])
26
27     # Flat-field correction
28     flat = np.mean(flat, axis = 0)
29     dark = np.mean(dark, axis = 0)
30     num = proj-dark
31     den = flat-dark
32     proj = num/den
33
34     # Normalization
35     proj = np.divide(proj, np.max(proj))
36
37     # Phase retrieval
38     pixel_size = np.array([1.625, 1.625])*1e-6 # in m
39     distance = np.array([0.19]) # in m
40     energy = 21 # in keV
41     one_phase = []
42
43     for j in range(0,1801):
44         print("Phase " + str(j))
45         one_proj = proj[j, :, :]
46         shape = one_proj.shape
47
```

```

48     retriever = phaseretrieval.TIEHOM(delta_beta=3.7e-8/1.7e-10,
    ↪     shape=shape, pixel_size=[pixel_size[0], pixel_size[1]],
    ↪     distance = distance, energy = energy)
49
50     phase, attenuation = retriever.reconstruct_image(one_proj)
51     one_phase.append(phase[ None, :])
52     all_phases = np.vstack(one_phase)
53
54     # Save phases
55     np.save('/data/staff/tomograms/users/julia/Final
    ↪     Analysis/phase_data_STD.npy', all_phases)

```



```

1 # 3D reconstruction
2 import numpy as np
3 import matplotlib.pyplot as plt
4 import tomopy
5 from PIL import Image, ImageChops
6
7 # Open file
8 phase = np.load('/data/staff/tomograms/users/julia/Final
  ↳ Analysis/phase_data_STD.npy')
9
10 # Create theta
11 theta = np.pi/180*np.linspace(0., 180., 1801, endpoint=False)
12
13 # Padding
14 phase = np.pad(phase, ((0,0), (0,0), (1000, 1000)), "edge")
15
16 # Reconstruction
17 recon = tomopy.recon(phase, theta, center=1282.13+1000,
  ↳ algorithm='gridrec', sinogram_order=False, filter_name='None')
18
19 for i in range(190):
20     print("Next recon: ", i)
21     one_img = recon[i, :, :]
22
23     # float32 to uint16
24     one_img[np.where(one_img<-0.0309)] = -0.0309
25     one_img[np.where(one_img>0.004)] = 0.004
26     minimum = -0.0309
27     if minimum < 0:
28         one_img += abs(minimum)
29     maximum = 0.004+np.abs(minimum)
30     one_img = one_img/maximum
31     one_img = one_img * 2**16-1
32
33     # Create image
34     PIL_image = Image.fromarray(one_img)
35     PIL_image = PIL_image.rotate(270)
36
37     # Crop image
38     left = 1000
39     top = 1000
40     right = 3560
41     bottom = 3560
42
43     PIL_image_cropped = PIL_image.crop((left, top, right, bottom))
44
45     # Save image
46     PIL_image_cropped.save("/data/staff/tomograms/users/julia/Final
  ↳ Analysis/Paganin_Manual/tomo_{}.tif".format(i))

```